IN SITU RHEOLOGY OF THE OCEANIC LITHOSPHERE ALONG THE HAWAIʻIAN RIDGE

A THESIS SUBMITTED TO THE GRADUATE DIVISION OF THE
UNIVERSITY OF HAWAIʻI AT MĀNOA IN PARTIAL FULFILLMENT OF THE REQUIREMENTS
FOR THE DEGREE OF

MASTER OF SCIENCE

IN

GEOLOGY AND GEOPHYSICS

DECEMBER 2018

By

Alexandra W. Pleus

Thesis Committee:

Garrett Apuzen-Ito, Chairperson
Paul Wessel
L. Neil Frazer

Keywords: lithosphere rheology; Hawaiʻian Ridge; flexure; thermal rejuvenation

Acknowledgements

Abstract

The Hawaiian Ridge beyond the main islands is composed of volcanoes with a large range of sizes, all formed on lithosphere of about the same age. This provides an unusually favorable setting to use plate flexure observations to examine the rheology of the oceanic lithosphere under different load stresses and a nearly uniform age-dependent temperature structure. We carry out such a study using new and archived shipboard gravity and multibeam bathymetry, combined with satellite-derived gravity. Flexure is simulated using thin-plate theory with curvature-dependent flexural rigidity, the strength of which is limited by brittle failure in the shallow lithosphere and low-temperature plasticity in the lower lithosphere. Misfits between model and observed residual gravity anomaly are combined with prior information to obtain posterior probabilities for model parameters: the frictional coefficient for brittle failure μ_f, a pre-exponential factor F for modulating the strength of four flow laws for low-temperature plasticity, average topographic crustal density ρ_c, thermal age which controls the geotherm, and a regional horizontal compression perpendicular to the ridge axis. Results show that all of the low-temperature plasticity laws require substantial weakening ($F = 10^2 – 10^8$) when using a geotherm for the age of the surrounding seafloor (90 Myr). A relatively simple solution is that the Hawaiian hotspot has thermally weakened the lithosphere. Extreme thermal rejuvenation (40-50 Myr geotherm) is required for the dry low-temperature plasticity laws of *Mei et al.* [2010] and *Boioli et al.* [2015]. Moderate thermal rejuvenation (60-70 Myr geotherm) is required for *Katayama & Karato's* [2008] wet rheology. The dry flow law of *Kranjc et al.* [2016] in conjunction with minimal thermal rejuvenation (70-80 Myr) has highest probability and is thus our favored model for the Hawaiian Ridge.

Table of Contents

List of Figures

List of Tables

1. INTRODUCTION

Previous studies of the oceanic lithosphere have aimed to characterize the mechanical behavior of the lithosphere by examining its flexural response to topographic loads associated with volcanoes, at subduction zones, and at fracture zones [e.g., see *Watts* 1978, 2001; *McNutt & Menard* 1982; *Sandwell* 1984; *Parmentier & Haxby* 1986; *Wessel & Haxby* 1990; and references therein]. Using observations of topography combined with marine gravity or satellite altimetry, such studies have determined that the strength of the lithosphere—represented by the effective elastic plate thickness, T_e—increases approximately with the square-root of seafloor age at time of loading, confirming the importance of cooling and the thickening of the lithospheric thermal boundary layer on the long-term flexural strength of a plate [e.g., *Calmant* 1987; *McNutt & Menard* 1982; *Watts* 2001]. Along the Hawaiian-Emperor chain T_e has been estimated to be 20-30 km around the older volcanoes away from the Hawaiian Islands [*Watts* 1978] and 40 km among the main Hawaiian Islands [*Watts & ten Brink* 1989]. *Wessel* [1993] then found that using a constant elastic plate thickness in flexure models may underestimate the true values for the Hawaiian chain, and suggested a model in which T_e varies with curvature [*McNutt & Menard* 1982]. With this method, T_e was estimated at 44 km beneath the seafloor far from the Hawaiian Islands, decreasing to 33 km directly beneath the youngest island of Hawaii. The above studies of Hawaii demonstrate the common tendency for T_e to decrease with load age, which reflects the viscoelastic nature of the lithosphere [*Watts & Zhong* 2000; *Watts et al.* 2013].

To address the more complex and complete rheological behavior of the lithosphere, *Zhong & Watts* [2013] examined a series of three-dimensional, time-dependent models of lithosphere deformation beneath the main Hawaiian Islands. This study was motivated by a persistent deficit in our understanding of lithosphere rheology in part because deformation experiments at the low-temperature and high-stress conditions of the lithosphere are relatively sparse [e.g., *Mei et al.* 2010], and because the strong strain rate dependence introduces uncertainty when extrapolating results derived from laboratory strain rates (10^{-4} to 10^{-6} s^{-1}) to the much slower geologic strain rates (10^{-15} to 10^{-19} s^{-1}) [*Watts & Zhong* 2000]. *Zhong & Watts* [2013] (hereafter referred to as *ZW13*) took the alternative approach of investigating lithosphere rheology by using seismic observations of the flexed oceanic plate near the island of Oahu [*Watts & ten Brink* 1989] to test laboratory-derived deformation laws by explicitly simulating them in three-dimensional (3D), time-dependent finite element models of the lithospheric flexure beneath the Hawaiian Islands. Their focus was on brittle failure in the shallow lithosphere and low-temperature plasticity and high-temperature creep in the deep lithosphere.

Zhong & Watts [2013] found that, in order to explain the seismically imaged surface of the pre-existing oceanic crust as it flexes downward beneath Oahu [*Watts & ten Brink* 1989], the lithosphere required a much weaker rheology than determined in the laboratory.

In the low-temperature plasticity regime, the pre-exponential factor in the laboratory-derived flow law from *Mei et al.* [2010] had to be increased, and thus the strength weakened by 6-8 orders of magnitude for the modeled flexures to match the seismic observations. In the brittle regime, the value of the frictional coefficient μ_f in Byerlee's law was also inferred to be low compared to the standard value derived from the laboratory, 0.7 [*Kohlstedt et al.* 1995]; values of $\mu_f = 0.25\text{-}0.7$ were found to be most compatible with the distribution of seismicity associated with lithosphere flexure.

This study builds upon the work of *ZW13* by using a new multibeam bathymetry and shipboard gravity compilation to examine lithospheric flexure around the older volcanoes along the Hawaiian Ridge, west of and older than the main Hawaiian Islands. The Hawaiian Ridge is a valuable location for such a study because it contains a large diversity of volcano sizes, all of which formed on oceanic seafloor of approximately the same age (Figure 1). This situation provides a natural setting to explore the flexure of the oceanic lithosphere in response to a wide range of load stresses but at an approximately constant lithospheric thermal structure. In contrast, the study of *ZW13* was restricted to seismic profiles between Oahu and Molokai, an area influenced by the relatively large loads of the Hawaiian Islands. The advantage that *ZW13* had was a more accurate measure of flexure provided by seismic reflections of the deformed oceanic crust, whereas this study relies on indirect sensing of the crust-mantle interface from gravity data. The volcanoes of the Hawaiian Ridge in this study all have ages >5 Myr, so the short-term viscous stress relaxation following loading has mostly stopped [*Watts & Zhong* 2013]. Therefore, fast computational methods can be used to simulate static flexure in two-dimensional (2D) plan view, and we can explore a wider and more detailed range of parameter space than would be possible with models of 3D, time-dependent flexure.
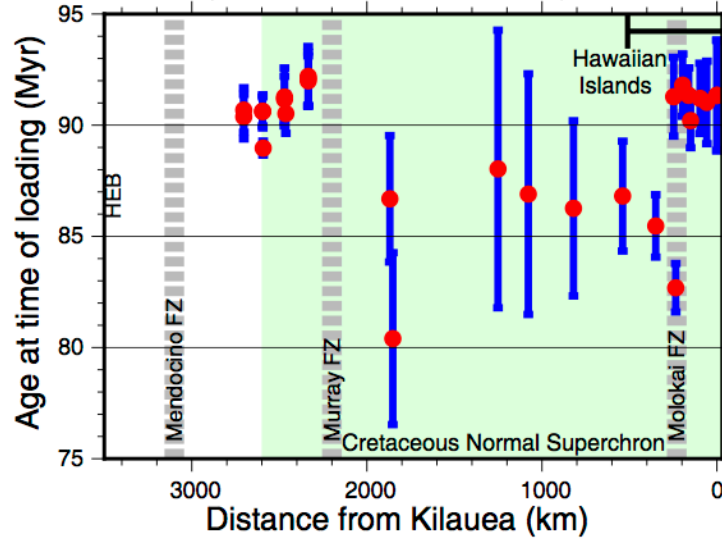
Figure 1: Ages of volcanoes and islands along the Hawaiian Ridge (map in Figure 2). Seafloor age at time of loading is found by subtracting volcano age [*O'Connor et al.* 2013, and references therein] from age of the surrounding seafloor. The age of the seafloor is found using magnetic isochrons [*Müller et al.* 2008]; error bars indicate uncertainty in seafloor age.

A potentially important shortcoming of the approach taken by *ZW13* is the assumption that the geotherm beneath Hawaii was that for normal, 85 to 92-Myr-old lithosphere, cooling as a semi-infinite half space. This geotherm may underestimate temperatures because the oceanic lithosphere is thinner than predicted by the half-space cooling model beneath seafloor of ages >70 Myr [*Ritzwoller et al.* 2004, *Schmerr* 2012]. Local seismic studies also provide evidence of abnormally thin lithosphere beneath the Hawaiian Islands associated with the excess temperatures and magmatism imposed by the Hawaiian plume [*Li et al.* 2004, *Ribe* 2004, *Laske et al.* 2011]. Therefore, it is possible that the required weakening found by *ZW13* is in part due to their modeled low temperatures. This study will test different geotherms to explore this possibility.

This study aims to quantify the most probable values for parameters that control the lithosphere's flexural response to a given load, and to investigate several published low-temperature plasticity flow laws. Parameters we explore are the coefficient of friction μ_f, the low-temperature plasticity pre-exponential F, crustal density ρ_c, and the thermal age of the lithosphere using the cooling plate model. The flow laws we test are *Mei et al.* [2010], *Kranjc et al.* [2016], *Boioli et al.* [2015], and *Katayama & Karato* [2008]. We also consider the influence of a SSW-NNW net compressive stress in the plate [*Ghosh et al.* 2013]. We conclude that some form of lithospheric weakening has occurred beneath the Hawaiian chain and thermal rejuvenation is likely to be an important factor.

2. BATHYMETRY AND GRAVITY DATA

2.1 BATHYMETRY DATA

Multibeam bathymetry and shipboard gravity data were collected along the Hawaiian Ridge in 2014 onboard the Schmidt Ocean Institute's *R/V Falkor* during a 72-day survey of the Papahanaumokuakea National Marine Monument. The *R/V Falkor's* multibeam system gathered high-quality multibeam bathymetry data primarily on the flanks and around the rims of the summits of the seamounts and small islands. These data were combined with other multibeam data by numerous expeditions compiled by the Hawaii Undersea Research Laboratory [*Smith & Kelley* 2010] and by the Hawaii Mapping Research Group's multibeam bathymetry closer to the main Hawaiian Islands (http://www.soest.hawaii.edu/HMRG/multibeam/). The combined data produced nearly complete coverage of the seamounts from the flexural moats to the rims of the shallow summits in water depths >50 m. Gaps in the shipboard multibeam bathymetry were supplemented with the 30-arc-second global topography/bathymetry grid SRTM30 PLUS [*Becker et al.* 2009]. Because we use bathymetry data to model gravity, we used only the grid points constrained by ship measurements, omitting those constrained only by satellite altimetry (which depend on gravity). Gaps were filled in with cubic spline interpolation using the *surface* routine from the Generic Mapping Tools, GMT [*Wessel et al.* 2013].

The bathymetry was then corrected for the regional effects of normal subsidence with seafloor age as well as the Hawaiian hotspot swell in order to create a residual bathymetry grid. We used the subsidence and swell predictions from *Wessel* [2016]. Thermal subsidence is caused by lithosphere cooling and thickening with seafloor age. The hotspot swell is caused by upwelling mantle material from the underlying plume, and its long-wavelength signal is found using the optimal robust separator (ORS) method [*Wessel* 1998], which divides the Hawaiian Ridge into regional (swell) and residual (edifice) components. After these corrections, the last modification was to remove shallow topography associated with volcanic edifices not related to the Hawaiian volcano chain. To do this, we removed all residual bathymetry data shallower than 400 m that are >200 km north and south of the Hawaiian chain (i.e., at coordinates $|y| > 200$ km in the oblique Mercator projection map, Figure 2). The largest feature removed is Necker Ridge, south of the chain, and at the northern regions of the Mid-Pacific Mountains. The final resulting residual bathymetry is thus designed to represent only the topographic loads of the Hawaiian Ridge and the associated flexural response of the adjacent seafloor. The residual bathymetry data was then down-sampled to a grid spacing of 5 km, produced by filtering and interpolating again using the GMT *surface* routine [*Wessel et al.* 2013]. A map of the residual bathymetry is shown in Figure 2a.

2.2 GRAVITY DATA

The shipboard free-air gravity data produced by an UNOLS BGM-3 gravimeter temporarily installed onboard the *R/V Falkor* are of high quality, showing an RMS crossover error of 0.424 mGal. We also compiled all gravity data from the NGDC database, emphasizing data collected since GPS navigation was made available to scientific voyages in 1990, the one exception being the *Farnella* cruises from 1988 to 1991 which produced extensive shipboard coverage of flexural moats and arches. To optimize the internal consistency of the shipboard gravity data we first corrected for crossover errors by using the *R/V Falkor* dataset as a reference. Ship tracks were first split into individual segments of consistent speed and direction. Crossover locations were identified as areas where a *Falkor* track and an NGDC track intersected. The crossing point was computed, and the gravity at that point was calculated for both segments. The NGDC tracks were then shifted by the mean difference from the *Falkor* data. NGDC data with crossover errors of >10 mGal were discarded. These corrected NGDC tracks were then used as a reference to correct other crossing NGDC tracks that did not cross the *Falkor* data. The process continued until there were no further crossover points. The final RMS crossover error is 4.20 mGal.

The gaps between ship tracks were filled with altimetry-derived gravity data [*Sandwell et al.* 2014]. However, near the steep flanks and summits of the volcanoes we chose to use only shipboard data. This was done by omitting satellite data at locations with bathymetry shallower than 4 km. The shipboard free-air gravity data were then shifted by the mean discrepancy with the coinciding satellite-derived values to produce the final free-air gravity grid.

We then corrected for the gravitational effects of bathymetry. We used Parker's [1972] spectral method with 6 terms in the series summation to find the gravitational attraction, g_z, of the observed bathymetry h_{obs}:

$$\mathcal{F}[g_z] = 2\pi\gamma e^{|K|z_{obs}} \sum_{n=1}^{6} \frac{(-|K|)^{n-1}}{n!} \mathcal{F}[\Delta\rho h_{obs}]. \tag{1}$$

Here K is the magnitude of the 2D wavenumber, γ is the gravitational constant, $\Delta\rho$ is the density contrast between the crust and water, and z_{obs} is the upward continuation height, optimally defined as the mid-depth between the deepest and shallowest points of the bathymetry. The Bouguer correction is therefore,

$$g_{b_{corr}} = g_z - \overline{g_z} - 2\pi\gamma\Delta\rho z_{obs}, \tag{2}$$

where $\overline{g_z}$ is the mean value of the computed bathymetric effect and the last term is the simple Bouguer plate contribution, which estimates the gravitational attraction of an infinite slab of density $\Delta\rho$ and height z_{obs}. The Bouguer correction is then subtracted from the observed free-air data to produce the complete Bouguer gravity anomaly.

We then calculated the residual Bouguer gravity anomaly. The residual Bouguer anomaly is the complete Bouguer anomaly with additional corrections for gravitational

effects from large wavelength regional features. The first such feature is the Hawaiian hotspot swell. The gravitational signal associated with the hotspot swell was calculated using Parker's method on three contributing components. The first component is the positive gravitational attraction of the crust-seawater interface, which has swell topography h_{swell} (the same used to produce residual bathymetry, again from *Wessel* [2016]). The upward-continuation distance $z_{obs,1}$ is the mid-depth of the swell bathymetry; the density contrast is $\Delta\rho_1 = \rho_{oc} - \rho_w$, where $\rho_{oc} = 2800$ kg/m³ is the mean the density of the oceanic crust [*Carlson et al.* 1988], and $\rho_w = 1000$ kg/m³ is the density of water. The second gravitational component associated with the hotspot swell is from the mantle-crust interface, which has the same shape h_{swell} as the crust-seawater interface. The upward-continuation distance is $z_{obs,2} = z_{obs,1} +$ the thickness of the crustal layer (7 km); the density contrast is $\Delta\rho_2 = \rho_m - \rho_{oc}$, where $\rho_m = 3300$ kg/m³. The third and final component of the swell is the negative contribution caused by the mass deficit from the hot, low-density mantle plume. The source of this compensating, negative density contrast below the lithosphere is the product of h_{swell} and $\Delta\rho_3 = \rho_w - \rho_m = -2300$ kg/m³. The upward continuation distance is $z_{obs,3} = z_{obs,2} +$ the thickness of the lithosphere, estimated to be 70 to 90 km [*Laske et al.* 2011]. The 20 km-uncertainty in the thickness of the lithosphere beneath the Hawaiian Ridge leads to a maximum uncertainty in the swell contribution to gravity of 7.24 mGal, which is later included in our observational error when calculating model likelihood.

The second long-wavelength signal we remove is a regional linear trend. A planar surface is fit to the complete Bouguer gravity anomaly minus the swell contribution. The resulting planar surface shows a total variation of 20 mGal, sloping with relatively high gravity values in the SSE and relatively low values in the NNW. This surface and the swell contribution are then subtracted from the complete Bouguer gravity anomaly.

As done for the residual bathymetry grid, it is also important to remove the effects of volcanic edifices unrelated to the Hawaiian chain. We removed all residual Bouguer anomaly values that are >200 km north and south of the Hawaiian chain (i.e., at coordinates $|y| > 200$ km in the oblique Mercator projection map, Figure 2) with residual bathymetry shallower than 400 m. Like the residual bathymetry grid, the residual Bouguer gravity grid was filtered and down-sampled to have a 5 km grid size.

The above modifications produce a gravity anomaly (Figure 2b) that primarily reflects subsurface density variations internal to the Hawaiian volcanoes (at wavelengths narrower than individual volcanoes) and associated with lithospheric flexure (at wavelengths comparable to the width of individual volcanoes and greater). To isolate the intermediate wavelengths associated with flexure, the residual Bouguer gravity grid was further filtered in the Fourier domain with a cosine taper between wavelengths of 300 km and 200 km. The wavenumber limits were chosen to eliminate short-wavelength

information (primarily due to internal density variations within volcanoes) in the observed gravity, while not altering the modeled gravity anomalies. For consistency, the same filter was applied to the model output with negligible impact. We will refer to this final, filtered residual Bouguer anomaly as the RBA. The RBA is sensitive to the shape of the flexed lithosphere. When a volcanic load causes the lithosphere to flex downward (or upward), the lower-density oceanic crust is pushed deeper into (or raised above) the higher-density mantle, and this contributes negatively (or positively) to the RBA. A map of the filtered RBA is shown in the results section where it is compared with model predictions.
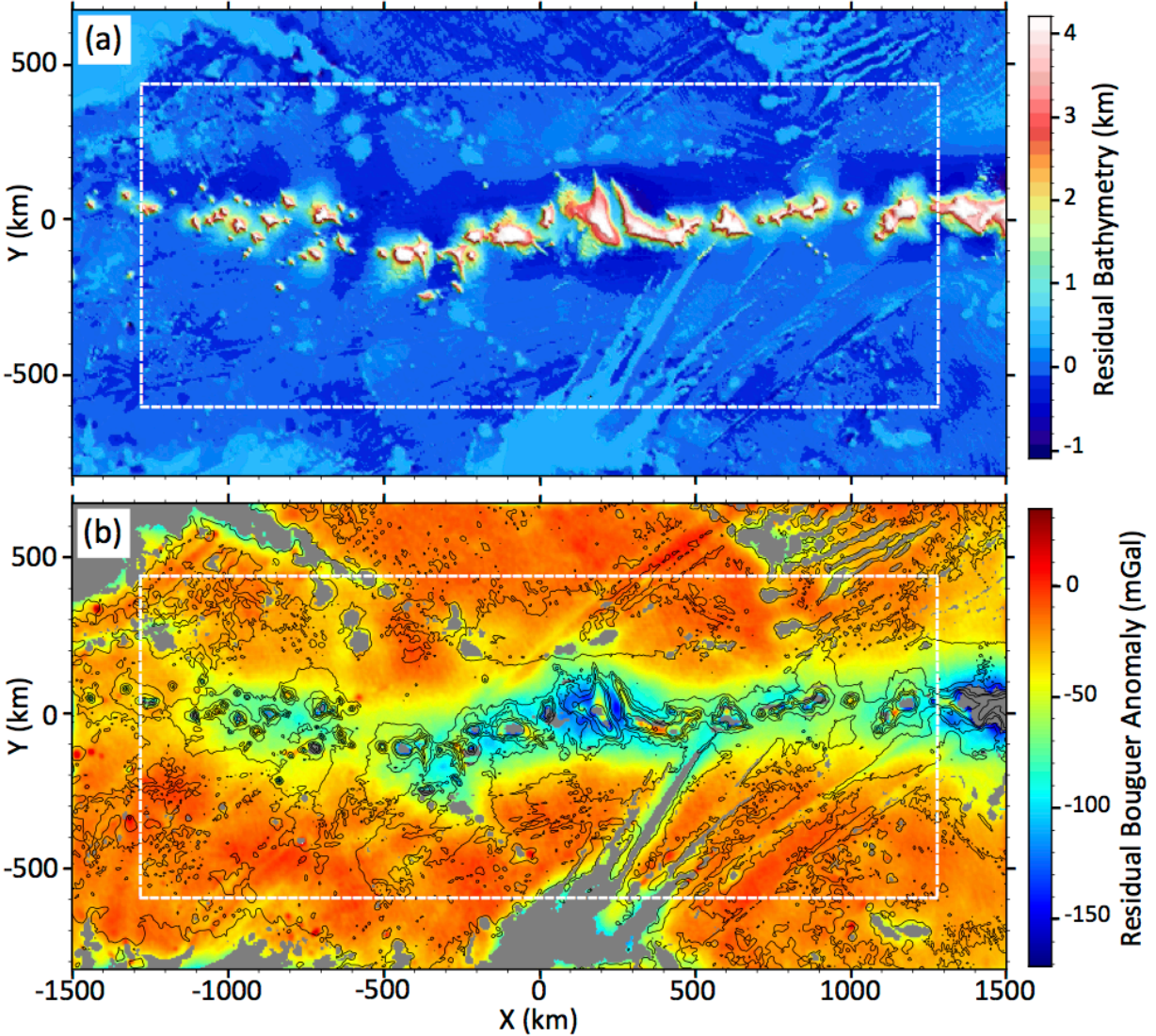
Figure 2: Maps of the data grids with 5 km grid size in oblique Mercator projection. (a) Residual bathymetry used as the topographic load in the flexure model. (b) Residual Bouguer anomaly before final Fourier domain filtering. Crustal density used for the Bouguer correction and in the flexure model is a model parameter; in this map, the density is 2600 kg/m^3. Contours of the residual bathymetry (black) are shown in intervals of 1 km. Gravity is predicted for the entire bathymetry grid, but the region of comparison is 200 km inward from each boundary (white dashed lines) to minimize edge effects from the 2D Fourier transforms.

3. FLEXURE MODELING AND METHOD OF SOLVING FOR RHEOLOGICAL PARAMETERS

To summarize the modeling procedure, the residual bathymetry is used as the surface load on the lithosphere, which we model as a thin elastic plate with curvature-dependent rigidity. The rigidity is controlled by the rheological model. The model residual Bouguer

anomaly is the gravitational signal of the crust-mantle interface as it undulates with the flexed lithosphere. We calculate model likelihoods, based on the fit of the model with observations, and then formally incorporate prior information to produce posterior probability density functions of the parameters that influence the flexure of the lithosphere (rheology, crustal density, plate age, far-field stress).

3.1 FLEXURE CALCULATIONS

The equation describing curvature-dependent flexure of a thin plate [*Timoshenko & Woinowsky-Krieger* 1959; *Wessel* 1993] is

$$D_0 \nabla^4 w + \Delta\rho w = (\rho_c - \rho_w)gh_{obs} - F(R, w), \tag{3}$$

where w is the downward deflection of the lithosphere, ρ_c is crustal density, ρ_w is density of seawater (1000 kg/m^3), h is the topographic load (the residual bathymetry), and g is the acceleration of gravity (9.8 m/s^2). D is the flexural rigidity of the lithosphere, which varies in space with the effective elastic plate thickness, T_e, according to

$$D(x, y) = \frac{ET_e(x,y)^3}{12(1-v^2)}. \tag{4}$$

Flexural rigidity is separated into its mean and spatially varying part,

$$D(x, y) = D_0 + R(x, y). \tag{5}$$

The constitutive law relating curvature C to the bending moment M is

$$D(x, y)C(x, y) = M(x, y), \tag{6}$$

and curvature is found using the maximum eigenvalue of the matrix

$$\begin{bmatrix} \frac{d^2w}{dx^2} & \frac{d^2w}{dxdy} \\ \frac{d^2w}{dxdy} & \frac{d^2w}{dy^2} \end{bmatrix}. \tag{7}$$

Eq. (6) depends on the rheology of the lithosphere as quantified by the yield strength envelope (Figure 3). *Kohlstedt et al.* [1995] describe three primary deformation regimes in the lithosphere: frictional sliding along (brittle) fault planes in the shallow, low-temperature lithosphere; the transitional semi-brittle regime, with multiple deformation mechanisms; and plastic flow in the deep lithosphere, controlled by dislocation glide (low-temperature plasticity) from ~400-800°C, and diffusion and dislocation creep at temperatures greater than ~800°C. We simulate brittle failure which is governed by the coefficient of friction μ_f; low-temperature plasticity, the strength of which is governed by a pre-exponential term F; and power law creep at high temperatures >800°C (Figure 3). Semi-brittle deformation is not well understood and thus is not explicitly simulated; however, its effects are explored in models with a reduced value of μ_f compared to that of Byerlee's law.

Low-temperature plasticity flow laws are primarily determined from laboratory deformation experiments and vary depending on experimental methodology and conditions. We test four flow laws: *Mei et al.* [2010], *Kranjc et al.* [2016], *Boioli et al.* [2015], and *Katayama & Karato* [2008] (Figure 3). *Mei et al.* [2010] used a multi-anvil press

('deformation-DIA'), to plastically deform polycrystalline olivine at pressures of ~4 to 9 GPa at $673 \leq T \leq 1273$ K and anhydrous conditions to obtain a flow law under near-steady state conditions. *Kranjc et al.* [2016] performed nano-indentation experiments on both single crystal and polycrystalline olivine from 273 to 448 K under anhydrous conditions. Compared to the flow law of *Mei et al.* [2010], *Kranjc et al.'s* [2016] law differs primarily in that the pre-exponential term A is much larger; therefore the *Kranjc et al.* [2016] rheology is equivalent to the *Mei et al.* [2010] rheology, but with F decreased by ~2.7 magnitudes. *Boioli et al.* [2015] created a 2.5-D dislocation dynamics model combining low-temperature deformation experiments of *Demouchy et al.* [2013, 2014] and numerical models of intracrystalline plasticity in order to simulate dislocation creep for olivine under lithospheric conditions. *Katayama & Karato* [2008] used a Griggs-type apparatus to explore olivine deformation under water-saturated lithospheric conditions. The details of the brittle and ductile flow laws and values of specific parameters for the four low-temperature plasticity rheologies are given in the Appendix.

For the ductile flow laws, we assume a strain rate of $\dot{\varepsilon} = 10^{-19}$ s^{-1} as guided by the dynamic solutions of *ZW13*. This strain rate is lower than typically used in this sort of application [e.g., *Hunter & Watts* 2016], and so the ductile strengths simulated in this study are conservatively low. However, the effects of strain rate are straightforward to interpret in our results because ductile strength scales proportionally with $\dot{\varepsilon}$ and with F (Eq. A.2), so that an increase in magnitude in $\dot{\varepsilon}$ corresponds to an increase in magnitude in weakening factor F.
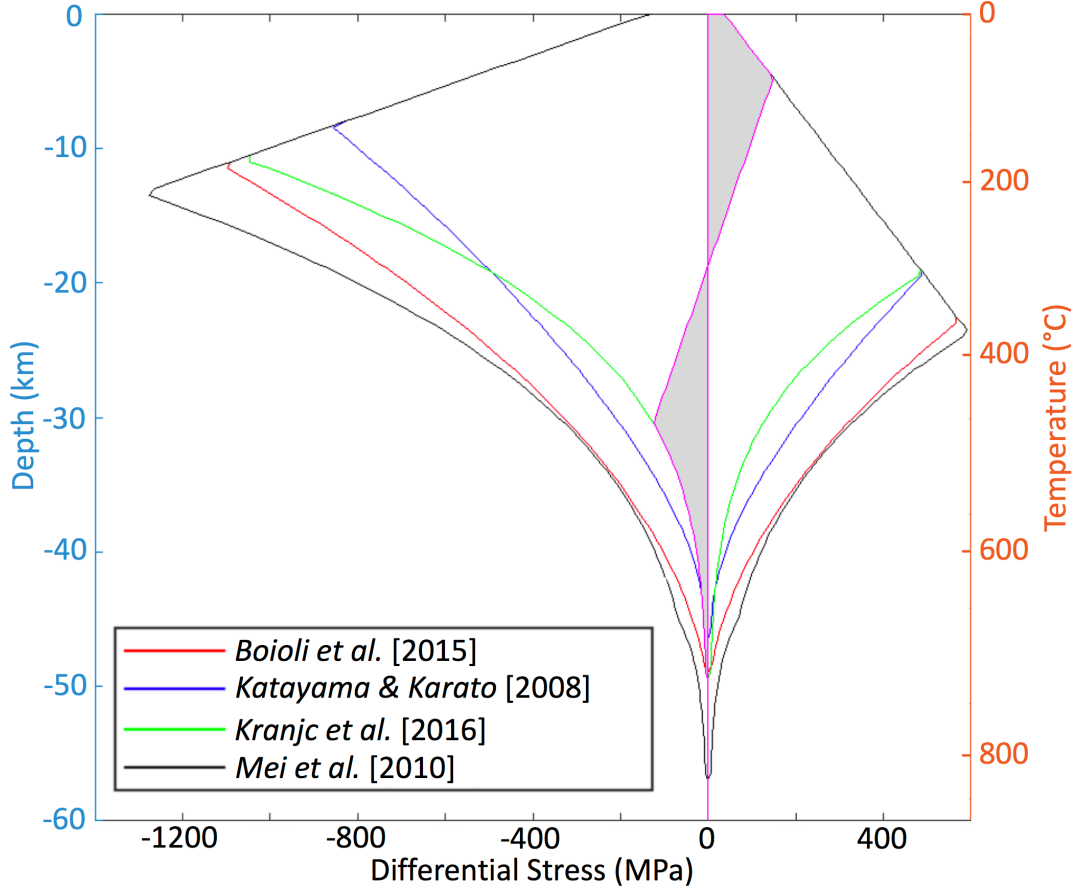
Figure 3: Yield strength limits for the four low-temperature plasticity flow laws tested (referenced in legend), shown here without any pre-exponential weakening ($F = 1$). The upper part of the yield envelope is limited by Byerlee's law for brittle failure, represented here with a frictional coefficient (μ_f) value of 0.7. At the greatest depths, we use a power law exponent of 3.5 for high-temperature creep. In the transition between low-temperature plasticity and high-temperature creep, which occurs between temperatures of ~600-800°C, stress is limited by the weaker of the mechanisms [*Hunter & Watts* 2016]. In this figure, strain rate is assumed to be 10^{-19} s⁻¹ and the geothermal gradient is that for *Parsons & Sclater's* [1977] plate cooling model for a 90 Ma geotherm. The pink line is the stress profile for a curvature of $+10^{-7}$ m⁻¹. The slope of the line interior to the yield envelope is proportional to curvature.

The differential stress profile (horizontal normal stress minus the vertical normal stress, positive corresponding to tension) is controlled by curvature. Under thin plate theory and for purely elastic deformation, curvature leads to a differential stress that is a linear function of distance from the middle neutral plane of the plate. Here, however, the linear profile is limited by the yield strength envelope (e.g., the pink line in Figure 3). The depth of the neutral plane z_n is defined so that the depth integral of the stress profile (i.e., the stress resultant) equals that imposed regionally by tectonic forces outside the model domain,

$$\int_0^{Z_{max}} \sigma(z)dz = \int_0^{Z_{max}} \sigma_0(z)dz. \tag{8}$$

Here the left-hand side is the depth integral of the yield-stress-limited differential stress profile and the right-hand side is the imposed tectonic stress resultant. With (8) providing, z_n, the solution for bending moment is

$$M(x,y) = \int_0^{Z_{max}} \sigma(z)(z - z_n)dz. \tag{9}$$

Given the computed values of $C(x,y)$ and $M(x,y)$, we then solve for flexural rigidity D with Eq. (6).

The dependence of D on curvature C, and thus on w, introduces a nonlinearity into Eq. (3), and so Eq. (3) through Eq. (6) must be solved iteratively. We did this by solving for w in the Fourier domain, and using Picard iterations to make successive approximations of the nonlinear term on the right hand side of Eq. (3). Iteration continued until the normalized residual (the L^2-norm of the difference between the left-hand side and right-hand side of (3) normalized by the right-hand side) was $< 10^{-2}$, or for 50 iterations, whichever came first. With the above accuracy achieved, the final solution for w is

$$w = \mathcal{F}^{-1}\left[\frac{\mathcal{F}[\rho g h_{obs} - F(R,w)]}{D_0 K^4 + (\rho_m - \rho_c)g}\right] \tag{10}$$

where $\mathcal{F}$ represents the 2D Fourier Transform and $\mathcal{F}^{-1}$ is the inverse Fourier Transform. The corresponding gravitational signal is the modeled residual Bouguer gravity anomaly,

$$g_b = \mathcal{F}^{-1}[2\pi\gamma(\rho_m - \rho_c)e^{-2\pi K z}\mathcal{F}[w]]. \tag{11}$$

All of the above equations were solved using MATLAB. As mentioned above, the final model signal was filtered as done to produce the filtered residual Bouguer gravity anomaly (RBA). Finally, to avoid edge effects of the 2D Fourier transforms, we defined a buffer zone that extends 200 km from each edge of the observed and modeled RBA grids. Our quantitative comparisons between the two grids are based only upon the area inside these buffer zones (see Figure 2).

3.2 LIKELIHOOD AND POSTERIOR PROBABILITY DENSITY FUNCTIONS

The misfit between the observed and modeled RBA was incorporated with Bayes' Rule to find relative probability density functions (PDFs) of the model parameters of the Hawaiian lithosphere. Such a method provides more complete information about the solutions than the more-commonly-used maximum likelihood methods. Bayes' Rule relates the desired posterior PDF $p(\boldsymbol{m}|\boldsymbol{y}_{obs})$ to the likelihood $p(\boldsymbol{y}_{obs}|\boldsymbol{m})$ and the prior distribution $p(\boldsymbol{m})$ according to

$$p(\boldsymbol{m}|\boldsymbol{y}_{obs}) \sim p(\boldsymbol{y}_{obs}|\boldsymbol{m}) \times p(\boldsymbol{m}). \tag{12}$$

The likelihood represents the probability that the observed RBA (vector), $\boldsymbol{y}_{obs}$, results from the model $\boldsymbol{m}$ (parameter vector). The likelihood is therefore controlled by the misfit between the modeled and the observed RBA: a relatively low misfit would yield a high relative likelihood, and vice-versa. We assumed the model misfits have a normal distribution with standard deviations σ_i: therefore,

$$p(\boldsymbol{y_{obs}}|\boldsymbol{m}) = \exp\left(\frac{\Sigma(y_{obs,i}-y_{model,i})^2}{\gamma\sigma_i^2}\right) = \prod \exp\left(\frac{-(y_{obs,i}-y_{model,i})^2}{\gamma\sigma_i^2}\right). \qquad (13)$$

The summation and product sequence occurs over the number of RBA grid points. The standard deviation accounts for the uncertainties in the observations and model predictions. Observational uncertainties are those associated with the final root-mean-squared crossover error of 4.2 mGal for the shipboard gravity data, and the 7.2 mGal uncertainty associated with the uncertainty of lithosphere thickness (70-90 km) used for the swell gravity. The form of (13) is based on the assumption that observations and errors are independent; however, flexure introduces spatial coupling on the scale of the flexural wavelength implying the number of degrees of freedom is well less than the number of (5 km $\times$ 5 km) RBA grid points. We therefore incorporate an additional term that modifies σ_i^2. The residual bathymetry map shows that the flexural arch extends approximately 200 km away from the seamounts, so we use 200 km as the minimum length scale for spatial decoupling. By approximating the decoupling area as (200 km)^2, a more accurate estimate of the degrees of freedom is incorporated by multiplying σ_i^2 by $\gamma = (200 \text{ km})^2/(5 \text{ km})^2$ in (13).

The model parameters that we solve for include the coefficient of friction in Byerlee's law for brittle failure, μ_f; the weakening factor F on the laboratory-derived pre-exponential term of the low-temperature plasticity flow laws; and the average density of the residual bathymetric load, ρ_c. To explore the possible thermal impacts of the Hawaiian hotspot, we also solve for thermal age t of the lithosphere, which controls the geotherm based on the *Parsons &* Sclater [1977] plate cooling model. Finally we examine the effects of different far-field, tectonic stresses in the lithosphere (see Eq. (8)).

The prior probability distribution is a product of prior distributions for all individual parameters in $\boldsymbol{m}$:
$$p(\boldsymbol{m}) = p(m_1) \times p(m_2) \times \ldots \times p(m_n). \qquad (14)$$

The prior distributions reflect our knowledge about each parameter from previous studies. For example, we know that the coefficient of friction in Byerlee's law must be positive and most likely near 0.7 [e.g., *Byerlee* 1978]. Semi-brittle deformation, however, can reduce the effective slope of the shallow yield strength envelope [*Kohlstedt et al.* 1995]. The prior probability is thus defined using a beta distribution centered on $\mu_f = 0.5$ and decreasing to 0.5 at values of 0.05 and 0.95 (Figure 4a). The pre-exponential weakening factor is most likely to be near 1 for the rheology of *Mei et al.* [2010], but *Zhong & Watts* [2013] needed weakening by 6-8 orders of magnitude. Therefore, the (beta) prior probability is defined to be greatest at $F = 1$ and decreases with increasing F to 0.1 near $F = 10^6$ (Figure 4a).

(a)

$\log_{10}(F)$

Prior probability

Coefficient of friction μ_f

(b)

Thermal age (Myr)

Crustal Density (kg/m^3)

(c)

Prior Probability
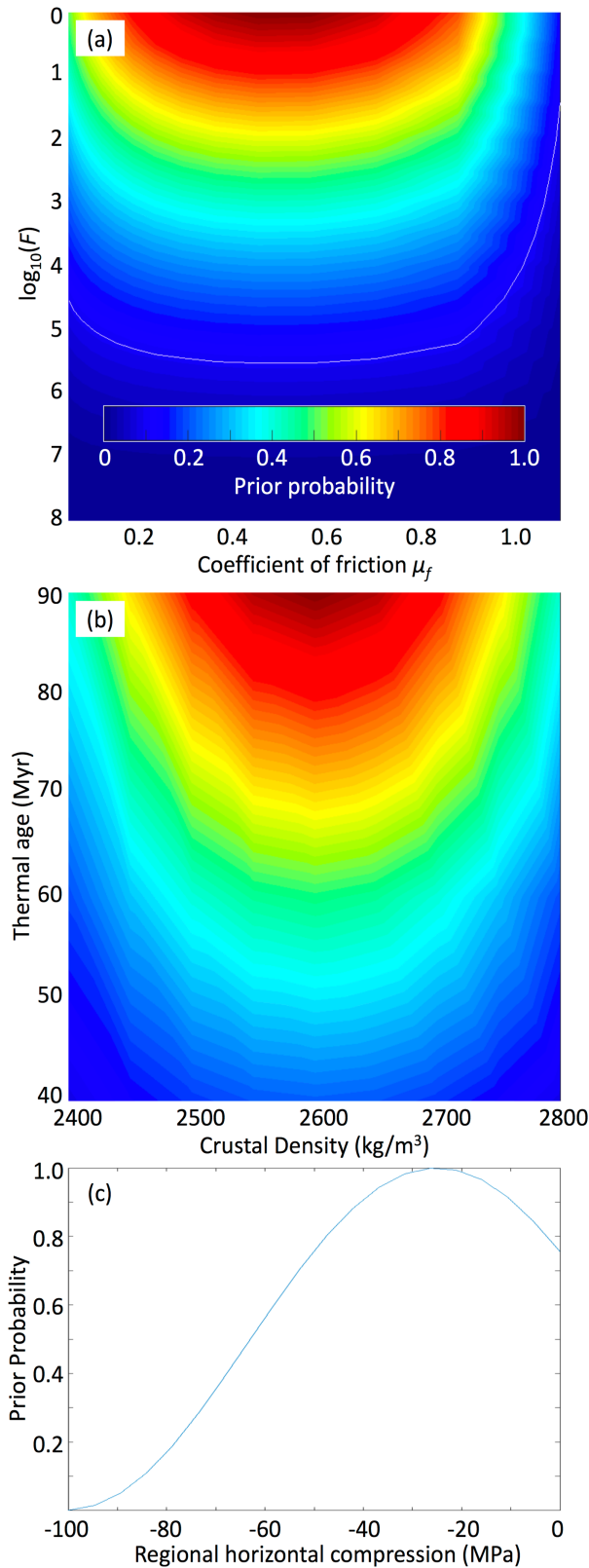
Regional horizontal compression (MPa)

Figure 4: Prior probability distributions for five model parameters as labeled.

In this study, we solve for the optimal average crustal density associated with topography, but true crustal density is not homogeneous. The topographic load is composed of dense basaltic lava rock, and a low-density carbonate rocks on the shallow summits of volcanoes [*MacDonald et al.* 1983], as well as low-density (~2300 kg/m^3) sediments infilling the flexural moats [*Watts & ten Brink* 1989]. *Watts & ten Brink* [1989] explored numerous models for the main Hawaiian Islands to explain the seismically imaged, flexed surface of the oceanic crust. Their models with a uniform density produced optimal fits to the flexed surface of the top of the oceanic seafloor with a mean density of $\rho_c = 2600$ kg/m^3. We therefore center our shifted and scaled beta distribution for crustal density on $\rho_c = 2600$ kg/m^3, decreasing the prior probability to 0.5 at 2400 kg/m^3 and 2800 kg/m^3 (Figure 4b).

To construct a prior probability distribution for thermal age, we incorporated information provided by the heatflow data compiled around the Hawaiian chain by *DeLaughter et al.* [2005]. From the Hawaiian Islands and across our study area, the observed heatflow values scatter about the model value of 53 mW/m^2 predicted by *Parson & Sclater's* [1977] plate cooling model for 90-Myr-old lithosphere. A few of the heatflow values are less than 53 mW/m^2 but the majority of them are within 20-30 mW/m^2 in excess of the model value. For a thermal age of 40 Myr, heatflow is predicted to be 79 mW/m^2, which is near the upper limit of the above range. Therefore, we center our prior for thermal age on 90 Myr, and decrease it to 0.2 at 40 Myr (Figure 4b).

Finally, we center our prior for the regional tectonic stress on the value for the Hawaiian Ridge found by *Ghosh et al.* [2013] of 25 MPa of horizontal compression. The prior probability decreases to 0.2 at ±50 MPa from the peak (Figure 4c).

To find posterior PDFs for the model parameters, we used the grid sampling method. We created a discretized grid in the parameter space, where each point in the grid designates specific values for each parameter. We modeled the flexure and RBA for each combination of parameter values and calculated the relative likelihood (Eq. 13, normalized by the greatest likelihood). Then, the relative likelihood grid is multiplied by the prior distribution $p(\boldsymbol{m})$ to obtain the relative (normalized by the maximum as computed by Eq. 12) posterior PDF. The relative posterior PDFs for each parameter provide the most probable model values for the Hawaiian Ridge and their formal uncertainties.

4. MODEL RESULTS

4.1 INITIAL ANALYSIS OF ELASTIC PLATE THICKNESS

Before solving the curvature-dependent problem for the rheological properties of the lithosphere, we begin with a traditional analysis of solving for the optimal uniform effective elastic plate thickness T_e. This is done to provide a comparison with prior T_e estimates and to inform future studies that focus on T_e. Upon testing T_e values of 6-37 km and crustal densities of 2400 – 2800 kg/m³, we find that $T_e = 27 \pm 4$ km and $\rho_c = 2600 \pm 100$ kg/m³ produce likelihoods within one standard deviation of the maximum (Figure 5). This optimal T_e range is in agreement with the range of $T_e = 17\text{-}37$ km for the Hawaiian Ridge from *Watts* [1978].

To identify any variations in T_e along the chain, we separate the study area into 4 sections of increasing load age (i.e., East-to-West), and calculate the best fit T_e value for each zone, varying T_e by intervals of 0.2 km. Crustal density is held constant at 2700 kg/m³. We find no significant change in optimal T_e value with smaller study areas: the values vary by ±0.8 km but do not change systematically across the chain with increasing load age, nor is there a clear dependence on load size. *Kalnins & Watts* [2009] used satellite-derived gravity and found T_e values of 13-27 km beneath this portion of the Hawaiian chain coinciding approximately with the depth to the 310 ± 120°C isotherm, rather than the 450°C isotherm as suggested by *Watts* [1978]. Using the *Parsons & Sclater* [1977] plate cooling model, the depth to 310 ± 120°C is 20 ± 8 km for 90-Myr-old lithosphere. Our estimate of 27 km is at the higher end of that range.
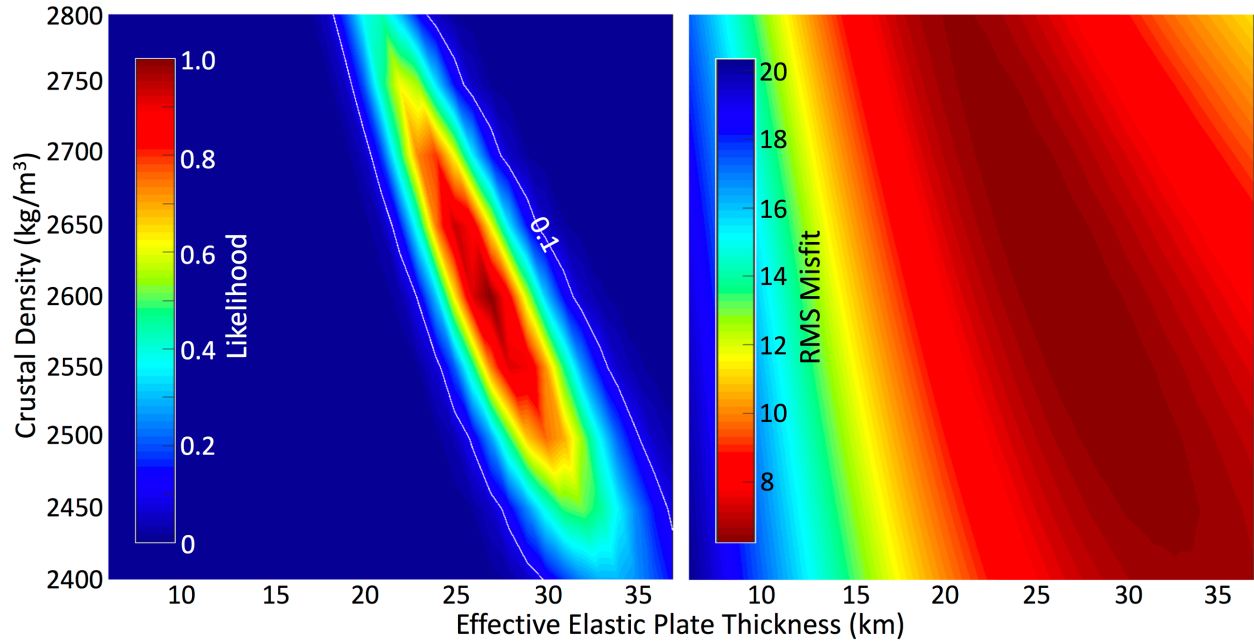
Figure 5: (a) Likelihood for different values of T_e and ρ_c and (b) RMS misfits of model and observed RBA. T_e varies in 1 km intervals; ρ_c varies in 50 kg/m³ intervals. The likelihood is normalized so the maximum value is 1.0.

4.2 COMPARISON OF DIFFERENT EXPERIMENTAL FLOW LAWS

First, we present results for the coefficient of friction μ_f, low-temperature plasticity weakening factor F, and crustal density ρ_c for the four experimentally-derived flow laws. The grid search included fifteen μ_f values evenly distributed in natural log-space from 0.05 to 1.10, and seventeen values of F distributed in $\log_{10}$-space from 1 (no weakening) to 10^8 (8 orders of weakening). Crustal density was tested in increments of 50 kg/m³ from 2400 to 2800 kg/m³.
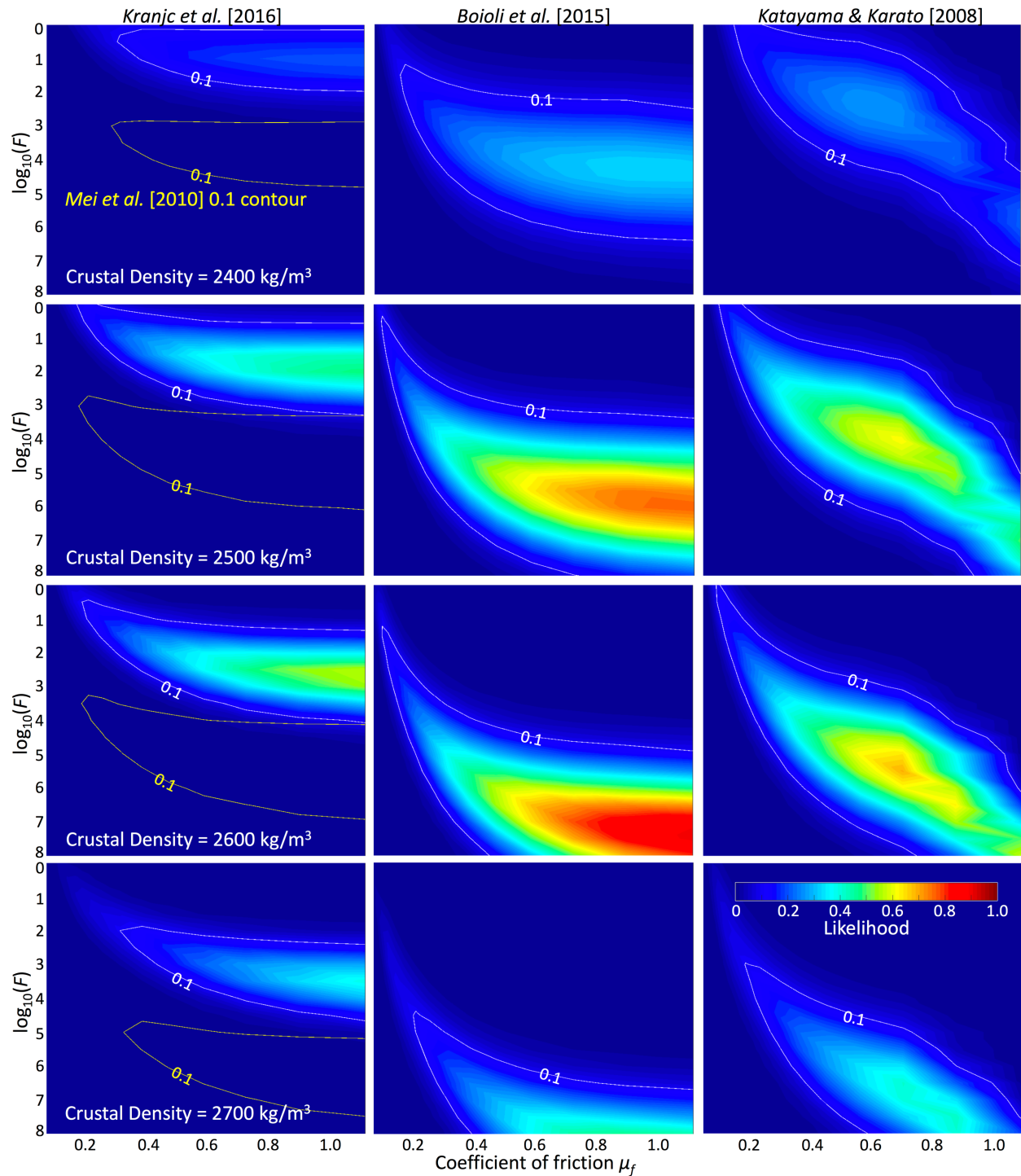
Figure 6: Likelihoods for different crustal densities (for each row as labeled) and experimentally-derived low-temperature plasticity flow laws: left column, *Kranjc et al.* [2016]; middle, *Boioli et al.* [2015]; right, *Katayama & Karato* [2008]. The strength of low-temperature plasticity decreases downward with increasing weakening factor F. Results for the *Mei et al.* [2010] rheology are represented by the yellow 0.1 relative likelihood contours in the panels on the left column.

For all flow laws, the zone of highest likelihood favors an increase in μ_f with decreasing strength of the low-temperature plasticity flow law (i.e., as μ_f increases, the weakening factor F also increases). In order to maintain approximately the same amplitude and wavelength of flexure, a greater brittle strength would require counteraction by a weaker low-temperature plasticity, and vice-versa. For the dry flow laws (*Mei et al.* [2010], *Kranjc et al.* [2016], and *Boioli et al.* [2015]), the zone of highest likelihood remains nearly constant in F as μ_f increases beyond ~0.5, and likelihood continuously increases with higher values of μ_f, indicating that the dry rheology models tend to favor smaller spatial variations in flexural rigidity (and effective elastic plate thickness T_e). We restrict our analysis to the shown range because, again, semi-brittle creep tends to reduce the effective slope of the strength envelope at shallow depths relative to $\mu_f = 0.7$ for Byerlee's law [*Kohlstedt et al.* 1995] as accounted for by our prior probability distribution for μ_f.

The likelihoods for the wet rheology *Katayama & Karato* [2008] peak at $\mu_f = $ ~0.7 and $F = $ ~10^5, but the zone of high likelihood shows a more steady increase in F with increasing μ_f, than the dry rheologies, which flatten out at higher μ_f. This result reflects the yield stress increasing more gradually with decreasing temperature and depth compared to the dry rheologies (Figure 3), and therefore increasing μ_f requires a more steady increase in weakening by F than the other flow laws.

The best fits with the observed RBA consistently require several magnitudes of weakening in F (10^4 to 10^8), and relatively high values of μ_f (>0.6). The map of RBA for a high likelihood model for the *Kranjc et al.* [2016] rheology visually shows a good match with the observed RBA (Figure 7), with the most notable differences being near the remnant effects of Necker Ridge in the southeast (X = 200-600 km, Y < 0 km). We also show two less likely models that fall along the 10% likelihood contour, one that requires more weakening in F (7c) and the other requiring less weakening (7d). Beneath the chain, the amplitude of flexure, as reflected in the magnitude of the negative portion of RBA, is slightly larger for a stronger rheology (greater F), and slightly smaller for a weaker rheology (smaller F). Figure 7e shows a low likelihood model with likelihood of <0.1; the values for μ_f and F are too weak, so the flexure is too great in amplitude and too large in wavelength. Figure 7f shows a model for the laboratory values: $\mu_f = 0.7$ and $F = 1$. In this case, the amplitude of flexure is too small, and the flexural wavelength is too broad. This comparison illustrates the need for relative weakening in order to explain the observed RBA.
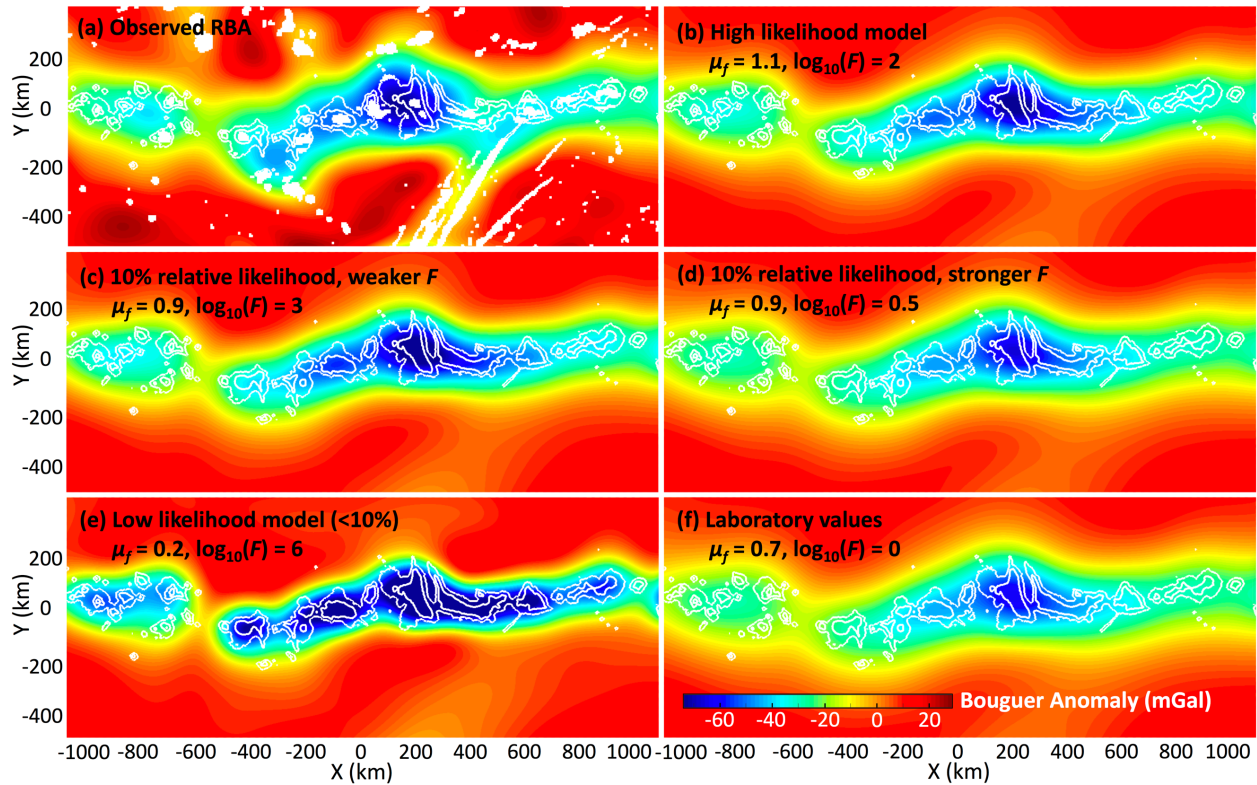
Figure 7: (a) The observed (filtered) RBA map for a crustal density of 2500 kg/m^3 compared with examples of model RBA maps using the same crustal density and the *Kranjc et al.* [2016] flow law. (b) The model with the peak likelihood for density of 2500 kg/m^3; (c) a model with 0.1 likelihood with a weaker rheology; (d) a model with 0.1 likelihood with stronger rheology; (e) a model with likelihood <0.1 with a rheology that is too weak; and (f) a model using the preferred laboratory-derived parameters. White contours show residual bathymetry in intervals of 2 km.
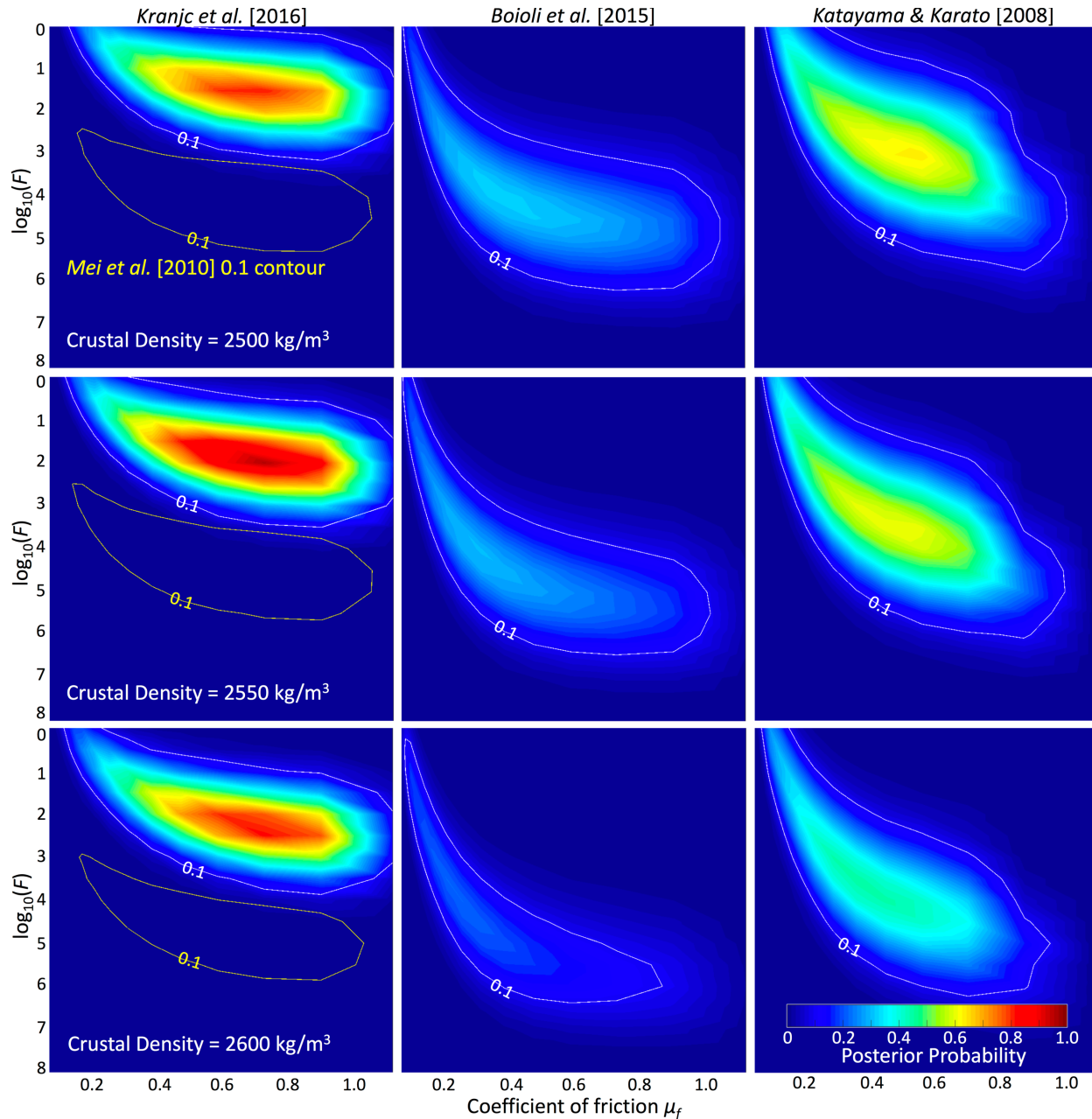
Figure 8: Posterior probability distributions for different densities (rows labeled) and low-temperature plasticity flow laws as in Figure 7. The posterior probabilities are normalized so that the largest of all shown in this manuscript is 1.0.

We are also able to qualitatively reproduce the results of *ZW13* for the Hawaiian Islands (also replicated in *Hunter & Watts* [2016]). Using *Parsons & Sclater's* [1977] cooling plate thermal model, the above results show that *Mei et al.'s* [2010] flow law must be weakened by 5-6 orders of magnitude. Instead, when using the semi-infinite half-space

cooling model, as *ZW13* did, the flow law requires a 7-8 magnitudes of weakening with $\mu_f = 0.7$. This amount of weakening closely matches that reported by *ZW13*.

The posterior probability distributions (Figure 8) show the effects of combining the prior information with the likelihoods (Eq. 12). We find that the flow law of *Kranjc et al.* [2016] has the highest posterior probability because it requires less pre-exponential weakening than the other 3 laws, with maximum probability of 1.0 at $\mu_f = 0.7$ and $log_{10}F = 2$. The highest likelihood models of the *Boioli et al.* [2015] at high μ_f and maximum weakening of F are no longer probable because of the low prior probability for high μ_f and such a large amount of weakening for low-temperature plasticity. Now, the *Boioli et al.* [2015] rheology has at most ~0.35 relative probability at lower values of μ_f (0.2 – 0.4) and larger values of $log_{10}F$ (3 – 5). Similarly, the *Mei et al.* [2010] rheology is also less probable, with peak probability of ~0.3 at $\mu_f = 0.6 – 0.7$ (weaker than favored in the likelihoods in Figure 6) and $log_{10}F = 4 – 5$ (larger than in Figure 6). The *Katayama & Karato* [2008] rheology shows a peak posterior probability of ~0.65 at moderate brittle strength ($\mu_f = 0.5$) and 3-4 magnitudes of weakening in F. Although our priors favored higher values of crustal density, the posteriors show highest probability at crustal density values of 2500 – 2600 kg/m³.

4.3 COMPARISON OF DIFFERENT GEOTHERMS

We now consider the possibility that the lithosphere has an anomalously hot geotherm due to the activity of the Hawaiian hotspot. We adjust the thermal age t of the *Parsons & Sclater* [1977] plate-cooling geotherm and compare results for minimal thermal rejuvenation ($t = 80$ Myr) to extreme thermal rejuvenation ($t = 40$ Myr).
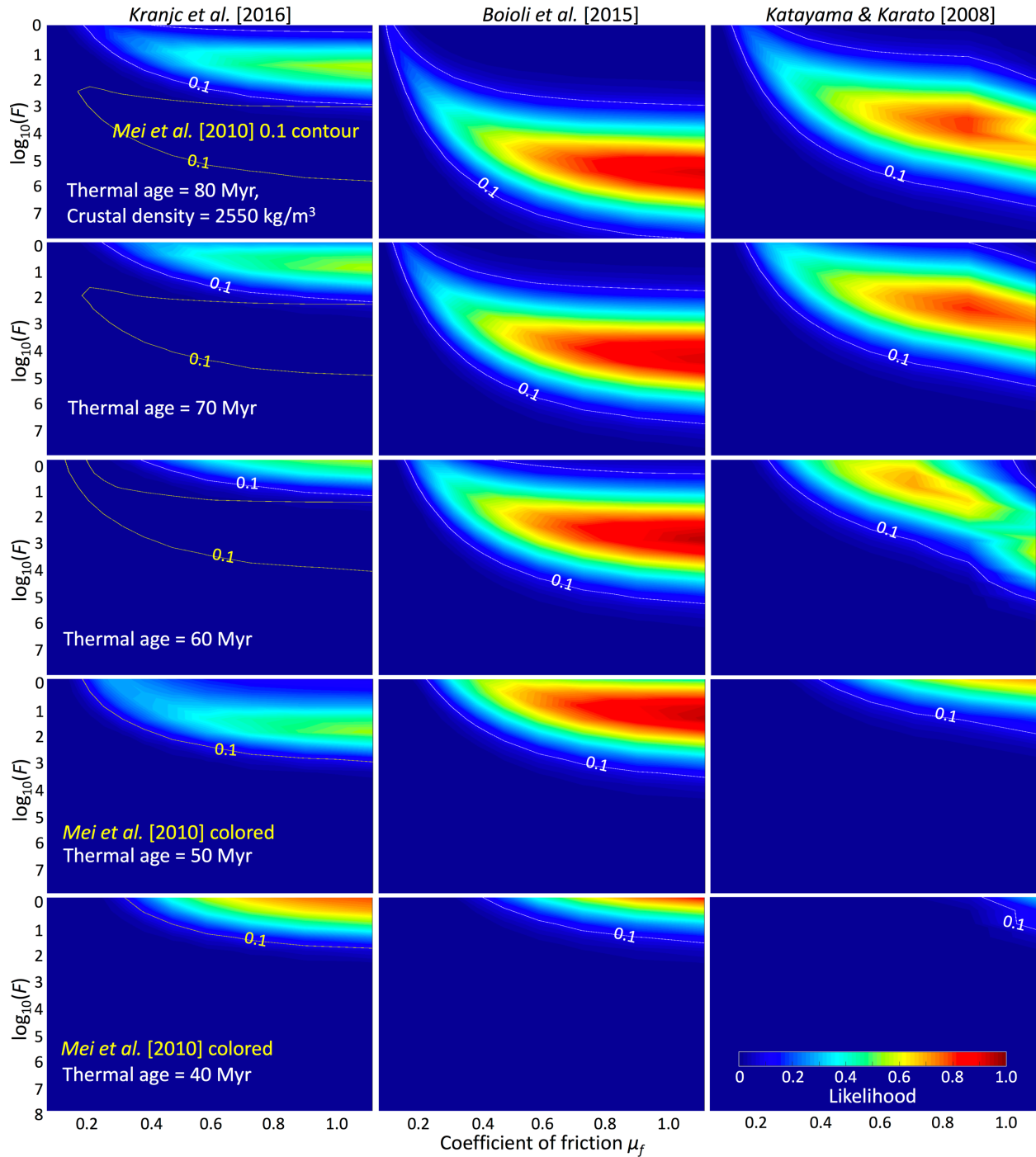
Figure 9: Likelihoods for geotherms of different cooling ages as labeled. Left column is for the flow law of *Kranjc et al.* [2016] (colored) with *Mei et al.* [2010] represented by the yellow 0.1 contour for ages 60-80. *Mei et al.* [2010] colored likelihoods are shown for ages 40-50, where the Kranjc 0.1 contour has values of $log_{10}F > 0$. Middle column is *Boioli et al.* [2015]. Right column is *Katayama & Karato* [2008]. Again, the likelihoods are normalized so the values here can be compared quantitatively to those in the other figures. Crustal density is constant at 2550 kg/m³, which showed greatest posterior probability.

Figure 10: Posterior probability distributions for geotherms of the three different thermal ages and flow laws as in Figure 9. Again, posterior probabilities are normalized so that the largest shown in this manuscript is 1.0. Crustal density is constant at 2550 kg/m³, which showed greatest posterior probability.

With increasing thermal rejuvenation (decreasing thermal age t), the zones of high likelihoods shift to smaller weakening factors F (Figure 9). At $t = 60$ Myr, the fl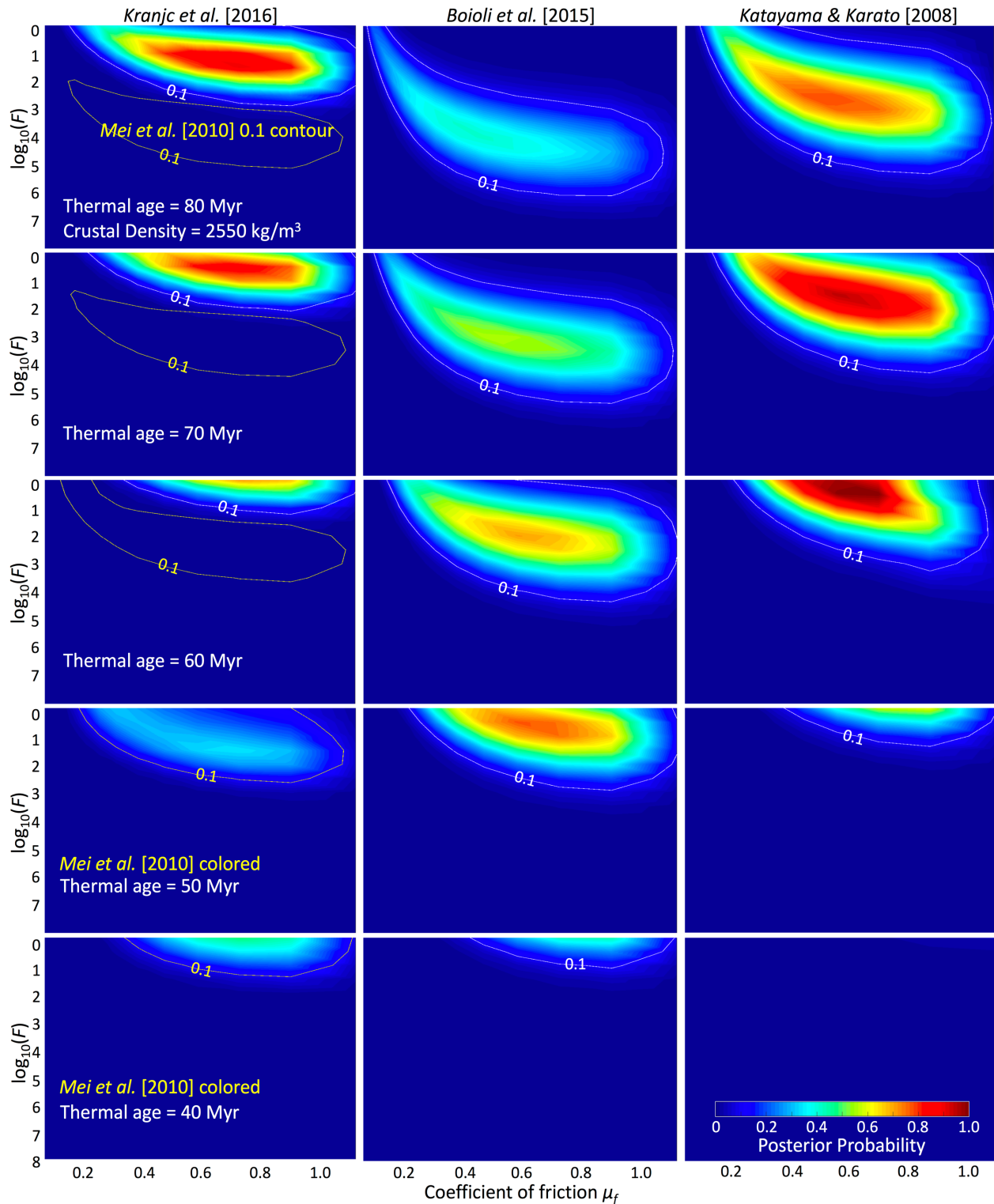ow laws of *Kranjc et al.* [2016] and *Katayama & Karato* [2008] require little to no weakening in F: the most likely values for $log_{10}F$ range from 0 to 1.5. The *Mei et al.* [2010] and *Boioli et al.* [2015] rheologies require no weakening in F for greater thermal rejuvenation to $t = 40$-50 Myr. Again, the flow law from *Boioli et al.* [2015] produces the highest likelihoods for all thermal ages, but at large values of weakening by F.

After incorporating prior information (Figure 10), we find that the greatest posterior probabilities are for modest thermal rejuvenation ($t = 60$-70 Myr) with the flow law of *Kranjc et al.* [2016]. With no weakening in low-temperature plasticity ($F = 1$), the *Kranjc et al.* [2016] rheology show moderately ($\geq$0.7) posterior probabilities at moderate frictional coefficients ($\mu_f = 0.4$-0.8). The flow law of *Katayama & Karato* [2008] has highest posterior probabilities ($\geq$0.8) for moderate thermal rejuvenation ($t = 60$-70 Myr), little weakening in low-temperature plasticity ($F = 1$-10^2), and moderate frictional coefficients ($\mu_f = 0.4$-0.8). The posterior probability is greatest at the slightly lower crustal density of 2550 kg/m^3 instead of 2600 kg/m^3, which has the greatest prior probability, because the flow law requires slightly less weakening in F. *Boioli et al.* [2015] has slightly lower posterior probability ($\sim$0.7) at similar ranges of parameter values as *Kranjc et al.* [2016] and *Katayama & Karato* [2008] ($\mu_f = 0.5$-0.9, $F = 1$-10^2), but more thermal rejuvenation is required ($t = 40$-50 Myr). *Mei et al.* [2010] has the lowest posterior probability, and at most only moderately probable ($\sim$0.4) with extreme thermal rejuvenation ($t = 40$ Myr), slightly higher frictional coefficients ($\mu_f = 0.6$-0.9), and no weakening ($F = 1$).

We examine the variation of the curvature-dependent effective elastic plate thickness T_e along the chain using a model of high posterior probability (Figure 11). T_e is weakest ($\sim$23-26 km) beneath the largest volcanic loads, where the upward curvature of flexure is greatest. T_e is moderately weak along the flanks ($\sim$27-35 km), where there is downward curvature. As the curvature flattens out away from the loads, the T_e values are strongest ($\sim$36-42 km). These large values are consistent with *Wessel's* [1993] model predictions for seafloor around the main Hawaiian Islands (40-44 km). His T_e predictions for flexing lithosphere directly beneath the volcanoes (35-40 km) are much greater than ours for the Hawaiian Ridge ($\sim$23-32 km). The main Hawaiian Islands are young, so viscous deformation beneath the loads is still active, and the plate is stronger. For several million years after loading, viscoelastic relaxation gradually reduces T_e [*Watts & Zhong* 2013]. This is consistent with the smaller values of T_e for the older loads of the Hawaiian Ridge. Our best-fit prediction for constant T_e (27$\pm$4 km) is within the range of T_e values for the Hawaiian Ridge where the plate is bending (23-30 km), so those areas control the shape of the flexed lithosphere.
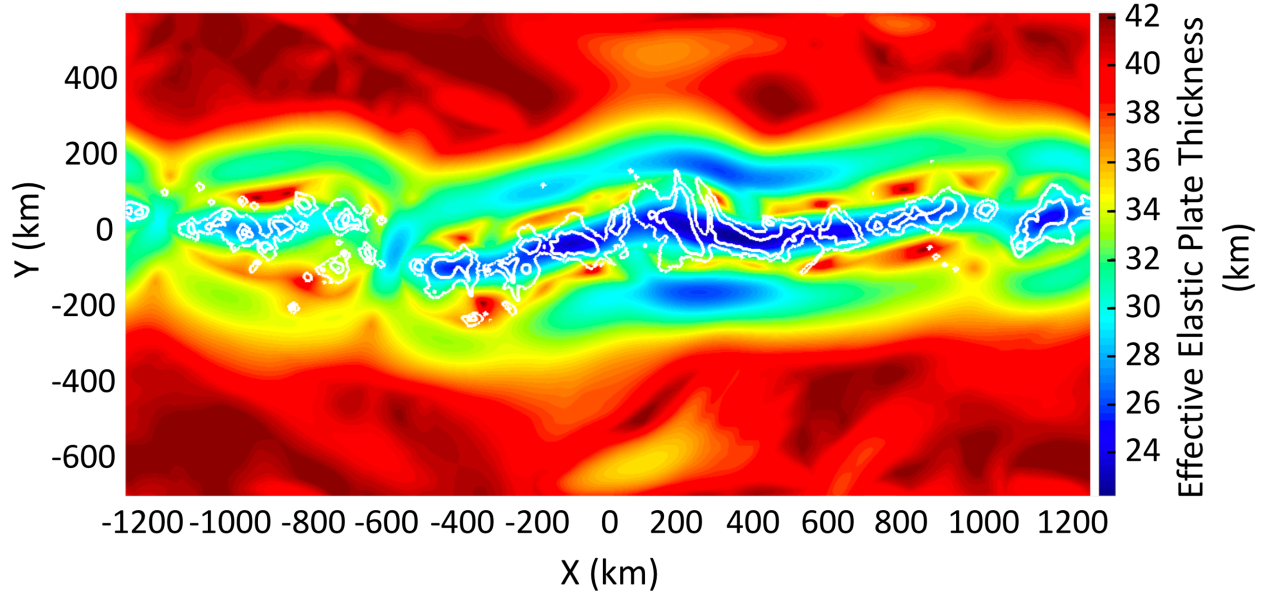
Figure 11: A map of variable effective elastic plate thickness T_e across the study area. Values were computed using a model with high posterior probability, as shown in Figure 10: $\mu_f = 0.7$; $log_{10}F = 0.5$; crustal density = 2550 kg/m³; $t = 70$ Myr; and the rheology of *Kranjc et al.* [2016].

4.4 REGIONAL TECTONIC COMPRESSION

Finally, we investigate cases of a regional horizontal normal tectonic stress in the lithosphere. A previous study by *Ghosh et al.* [2013] developed a model that coupled lithosphere mechanics and mantle convection to predict the global lithospheric stress field. Depth-integrated 3D force balance equations were solved—accounting for topography, lithosphere structure, and basal tractions from mantle convection—and constrained with observations from the World Stress Map and Global Strain Rate Model. Their results show moderate deviatoric stresses in the Pacific lithosphere around the Hawaiian Ridge, with a compressive stress (negative in our model) of 20-30 MPa in magnitude directed perpendicular to the Hawaiian chain. *Lowry & Smith* [1995] found that in some situations, a horizontal normal stress can affect the strength of the lithosphere during bending because the additional stress can cause thicker sections of the plate to be in brittle or ductile failure. Figure 12 illustrates that a compressive tectonic stress can increase the effective flexural rigidity D and T_e directly beneath a volcanic load where the lithosphere has concave up (i.e., negative) curvature (12c), but reduce D and T_e on the flanks of the volcano where the plate has concave down (i.e., positive) curvature (12b). In Figure 12b, the mean tectonic stress (dashed vertical line) is -100 MPa and the stress profile, which must integrate to zero, is further limited by the yield strength envelope. The size of the elastic core (the vertical length of the linear portion of the stress profile interior to the envelope, shaded grey in Figure 12) decreases relative to that in 12a. In Figure 12c, a negative curvature changes the slope of the linear part of the stress profile, so the size of elastic core increases relative to 12a.

The purpose is to test whether the effects of a net depth-integrated horizontal normal stress on the constitutive relationship between movement and curvature can contribute to the apparent weakness of the flexing plate beneath the Hawaiian Chain. However, we do not incorporate the effects of a net horizontal stress as an additional term in the momentum equation (Eq. 3). We present results for a wider range of potential tectonic stresses than estimated by *Ghosh et al.* [2013]: 25 MPa to 100 MPa of compression, in increments of 25 MPa. A crustal density of 2600 kg/m³, a geotherm of $t = 90$ Myr, and the *Mei et al.* [2010] and *Kranjc et al.* [2016] flow laws are used in all cases (Figure 13).
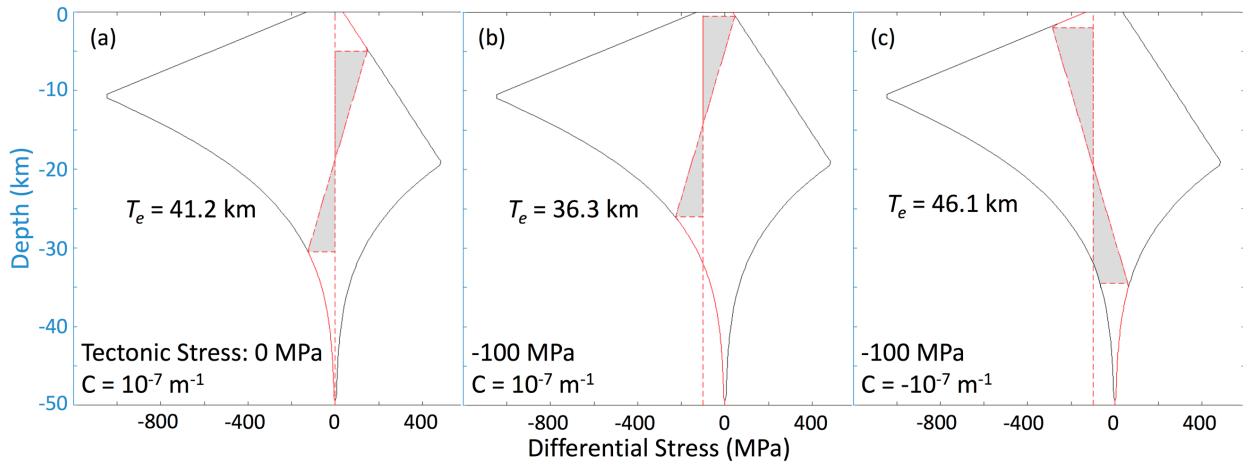
Figure 12: Three stress profiles associated with different effective elastic plate thicknesses for (a) 0 MPa of tectonic stress, and a positive curvature of 10^{-7} m^{-1}, which indicates tension on the top of the plate and compression on the bottom; (b) the same curvature with 100 MPa of compressive tectonic stress; and (c) 100 MPa of net compressive tectonic stress with 10^{-7} m^{-1} of negative curvature. Grey shading illustrates the elastic core, the area where the lithosphere undergoes purely elastic deformation and which supplies most of the strength of the plate in these examples.
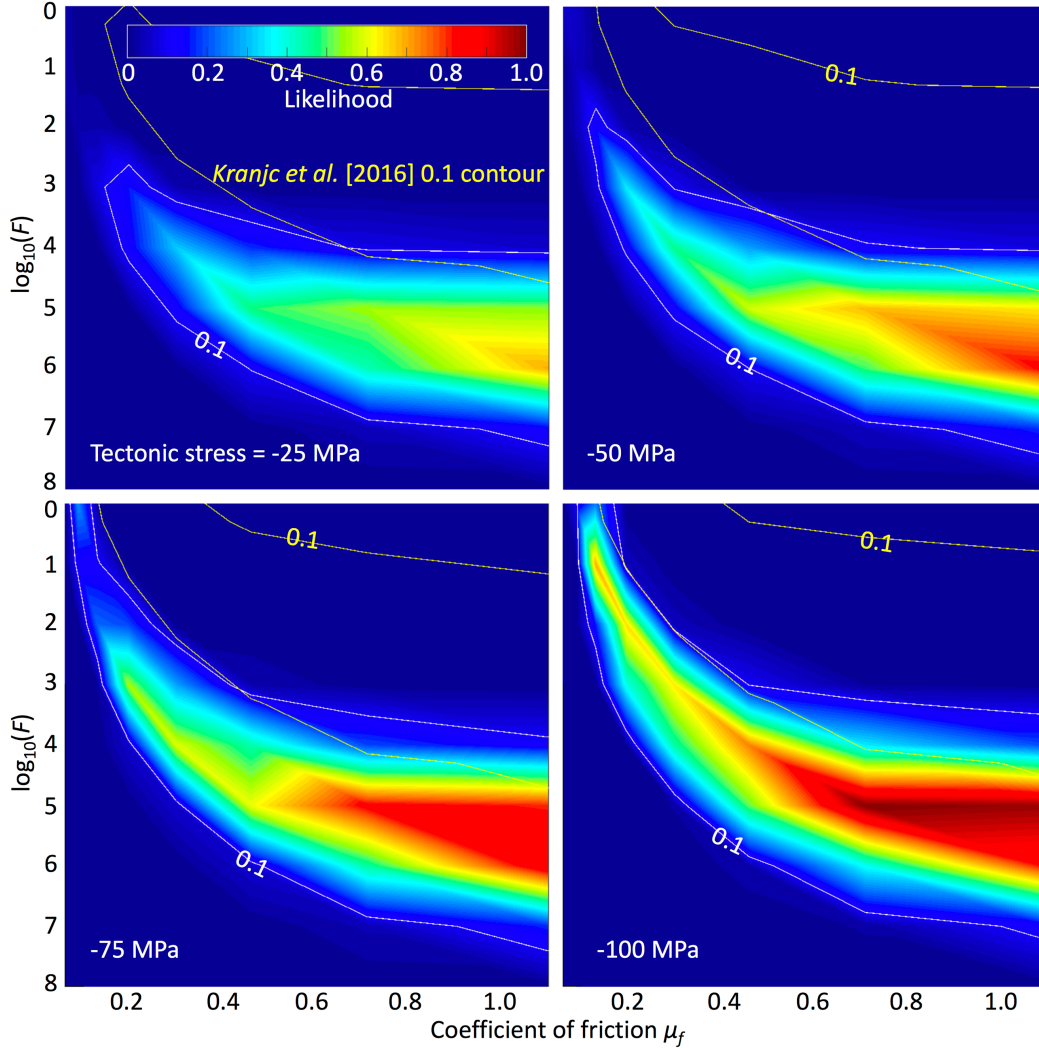
Figure 13: Normalized likelihoods for the *Mei et al.* [2010] (colors) and the *Kranjc et al.* [2016] (10% relative contour) flow laws for regional tectonic stress varying from 25 to 100 MPa of compression in increments of 25 MPa. All 4 likelihoods are normalized by the same maximum value as in Figure 6. Crustal density is a constant 2600 kg/m³.

The results for likelihoods show improved fits to the observations with increasing tectonic stress. Importantly, the zones of high likelihood follow the same trend of increasing F with μ_f regardless of tectonic stress (including zero stress). The most likely value for the frictional coefficient μ_f is still ≥0.7, similar to Figure 6, and the flow law of *Mei et al.* [2010] continues to need 5-6 magnitudes of plasticity weakening. The flow law of *Kranjc et al.* [2016] also requires the same amount of pre-exponential weakening (2-3 magnitudes) as the zero tectonic stress case. The posterior probability functions (Figure 14) show that the most probable value of μ_f shifts to very low values in order to reduce the amount of weakening required in F, which is preferred by the prior PDF for F. The model using 50 MPa of compression, *Mei et al.* [2010], and a 90-Myr geotherm has the highest posterior

27

probability at $\mu_f = 0.2$-0.3 and $log_{10}F = 3$-4.5. Overall, an increase in tectonic stress does not contribute to weakening D or T_e.
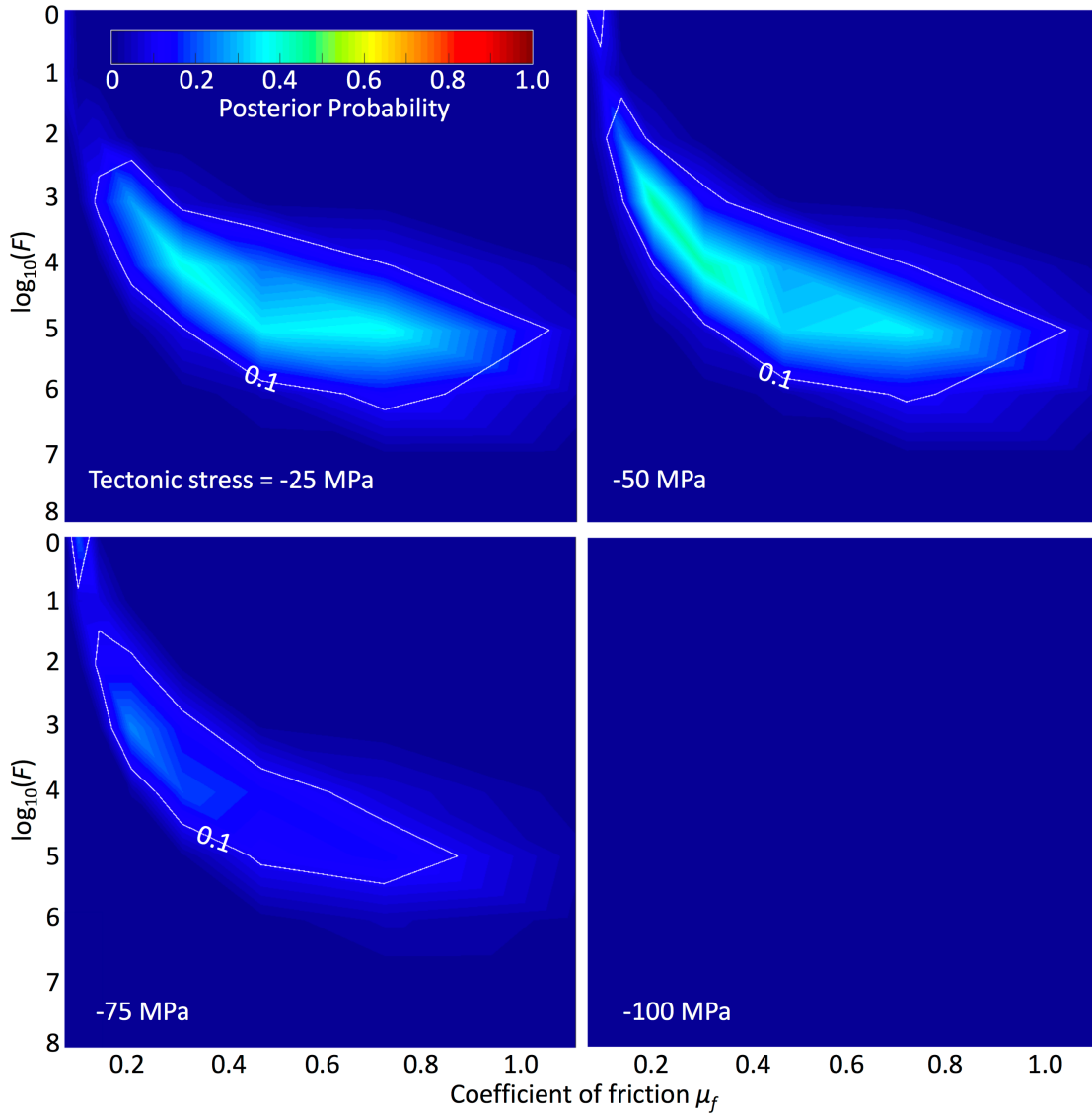
Figure 14: Normalized posterior probability distributions for the likelihoods shown in Figure 13.

5. DISCUSSION AND CONCLUSIONS

For a lithosphere thermal age of 90 Myr–equivalent to the seafloor age on which this part of the Hawaiian chain was constructed–we find that substantial weakening of the rheology is required compared to the published flow laws. There is a negative correlation between frictional coefficient μ_f and the strength of low-temperature plasticity, and so the weakening can occur through a lower value of μ_f with moderate weakening of F, or a larger

value for μ_f but more substantial weakening of F. A frictional coefficient value of ≥ 0.7 and 5-7 magnitudes of pre-exponential weakening, and crustal density ρ_c of 2500 – 2600 kg/m³ are the most probable values using a 90-Myr geotherm. The low-temperature plasticity flow law of *Kranjc et al.* [2016] has the highest posterior probability and has most probable values of $\mu_f = 0.5$-0.9 with 1-3 magnitudes of weakening of F. *Katayama & Karato* [2008] also has relatively high posterior probability, with most probable values of $\mu_f = 0.4$-0.6, and 3-4 magnitudes of weakening of F. Both *Kranjc et al.* [2016] and *Katayama & Karato* [2008] require ~3 magnitudes less pre-exponential weakening than *Mei et al.* [2010] and *Boioli et al.* [2015]. *Mei et al.* [2010] has relatively low posterior probability and has most probable values of $\mu_f = 0.4$-0.8 and 4-5 magnitudes of weakening in F; *Boioli et al.* [2015] also has low posterior probability with most probable values of $\mu_f = 0.2$-0.5 and 3-5 magnitudes of weakening in F.

Hunter & Watts [2016] estimated T_e for lithosphere at circum-Pacific subduction zones using a free-air gravity anomaly inversion. They then examined models of thin plate flexure to test whether the observed T_e values can be recovered when incorporating laboratory-derived brittle and ductile failure laws. Their main conclusions were that the curvature-T_e relationships found from the gravity observations could be well explained by the dry olivine rheologies for low-temperature plasticity of *Evans & Goetze* [1979], *Raterron et al.* [2004], and *Mei et al.* [2010] without the need for substantial weakening. *Mei et al.* 's [2010] rheology weakened by 4 orders of magnitude, as well as the wet rheology of *Katayama & Karato* [2008], produced fits to the observed T_e values just outside of the 95% confidence interval, suggesting that these flow laws are too weak. However, when the same method was applied to the Hawaiian Islands, they found *Mei et al.'s* [2010] flow law had to be weakened by 6-8 orders of magnitude, which also verified the results of *ZW13*. These findings combined with ours suggest that there is a process that causes the lithosphere around the Hawaiian Islands to be weaker for the same age of seafloor than the lithosphere subducting at the Pacific rim.

We then examined the effects of a regional horizontal compression perpendicular to the Hawaiian Ridge on the constitutive relation between curvature and bending moment. Our results demonstrate that even with extreme horizontal compression several times larger than estimated by *Ghosh et al.* [2013], non-zero regional tectonic stress still requires substantial weakening of the ductile flow laws. Thus it is not the effects of regional tectonic stress on the curvature-moment relation that can account for the apparent weakness of the Hawaiian lithosphere, although the effects on the momentum balance have yet to be tested.

We also investigated the possibility of thermal rejuvenation from the Hawaiian hotspot, which would cause the geotherm to become anomalously hot. The flow laws of *Kranjc et al.* [2016] and *Katayama & Karato* [2008] need little or no further weakening with

29

only moderate thermal rejuvenation (t = 60-70 Myr), and thus produce the greatest posterior probabilities. The *Mei et al.* [2010] and *Boioli et al.* [2015] rheologies without weakening have moderate to low posterior probability as they require greater thermal rejuvenation (40-50-Myr-old geotherm). Therefore, we favor the flow law of *Kranjc et al.* [2016] with moderate thermal rejuvenation (t = 60-70 Myr) for the Hawaiian Ridge. Because *Kranjc et al.* [2016] is equivalent to *Mei et al.* [2010] weakened by ~2.7 magnitudes, the unaltered flow law of *Kranjc et al.* [2016] is expected to fall within *Hunter & Watts*'s [2016] 95% confidence interval, which reconciles our results with circum-Pacific subduction zones.

As mentioned earlier, one constraint on the geotherm comes from seafloor heatflow observations. The theoretical heatflow values for a 60-70-Myr-old geotherm (64-70 mWm^{-2}) are within the upper range of observations adjacent to the Hawaiian Chain. These heatflow values were compiled by *DeLaughter et al.* [2005] from various sources, including *Von Herzen et al.* [1982, 1989] and *Harris et al.* [2000]. The theoretical heatflow excess relative to 90-Myr-old lithosphere (53 mWm^{-2}, meaning an excess of ~10-20 mWm^{-2}) is within the upper range of anomalies estimated by *DeLaughter et al.* [2005]. Hydrothermal circulation in the crust may also mask the observed heat flux, depressing values near the flanks of the volcanoes relative to actual mantle values [*Harris & McNutt* 2007]. An additional issue is that simulating thermal rejuvenation of the lithosphere by using a geotherm for younger seafloor is not entirely realistic. The excess heat from the hotspot reheats the lithosphere from below, so its effects are likely to be less in the shallow lithosphere and greater near the base of the plate than reflected in our models. The model geotherms with ages of 60-70 Myr therefore better represent the deeper plate temperatures that govern low-temperature plasticity than the near-surface temperatures which influence heatflow. Thus, our most probable model of moderate thermal rejuvenation cannot be rejected based on heatflow observations.

Other constraints on the geothermal structure of the lithosphere beneath Hawaii come from seismic observations. *Li et al.* [2004] mapped lithosphere thickness along and perpendicular to the Hawaiian Islands using S-receiver functions. They found the seismic lithosphere-asthenosphere boundary (LAB) becomes shallower with distance beneath progressively older islands up the chain from the hotspot: 100-110 km beneath Hawaii Island, as expected for 90- to 100-Myr-old lithosphere with no rejuvenation, to 50-60 km beneath Kauai. The depth to the 1000°C isotherm using the *Parsons & Sclater* [1977] plate cooling model is 74.5 km for 90-Myr-old lithosphere, which decreases to 62-67 km for 60-70 Myr, a difference of 7.5-12.5 km. This difference is much smaller than the 40-60 km of thinning found by *Li et al.* [2004]. In addition, surface wave tomography models from the Hawaii PLUME experiment [*Laske et al.* 2011] show that the fast S-wave speeds of the lithosphere shoal by ~20 km upon approaching Hawaii Island. This apparent reduction in lithosphere thickness persists to varying degrees along the chain. Thus, our estimate of

thermal thinning by 7.5-12.5 km is conservative compared to the evidence from the above seismic studies.

One possible cause of thermal rejuvenation is sub-lithospheric convection enhanced by the hot Hawaiian mantle plume. Early geodynamic modeling of the interaction between a mantle plume and the lithosphere simulating viscosity that changes only moderately with temperature predicted minimal thermal erosion of the cool, stiff underside of the lithosphere [*Ribe & Christensen* 1994]. Later numerical models that simulated larger viscosity variations and greater convective vigor demonstrated that small-scale convection near the base of the lithosphere can thin the lithosphere more substantially [*Moore et al.* 1998; *Ballmer et al.* 2011, 2013]. *Moore et al.* [1998] showed through numerical experiments that this convection is initiated even at modest plume temperatures (>100 K excess, relative to the background mantle). They also extrapolated the heatflow measurements of *Von Herzen et al.* [1989] to lithosphere temperatures of 750-900 K at 27 km depth 1100 km downstream from the plume origin; the *Parsons & Sclater* [1977] model predicts temperatures of only 693 K for standard 90-Myr-old lithosphere at 27 km depth. Results from the Hawaii PLUME experiment suggest that sub-lithospheric convection removes cool material from the base of the plate. The seismic tomography imaged hot plume material beneath the islands as a body of unusually low seismic wave speeds; the tomography also revealed regions of unusually high seismic wave speeds on the northeast-to-southwest side of the shallow plume material [*Wolfe et al.* 2009]. *Wolfe et al.* [2009] interpreted the seismically fast regions as being cool material that was removed from the base of the lithosphere and is now downwelling around the plume material, as predicted by geodynamic models [*Moore et al.* 1998; *Ballmer et al.* 2011, 2013].

Both thermal and mechanical weakening of the plate can also result from magma penetrating the lithosphere. Thermal weakening occurs as magma directly advects excess heat into the lithosphere. The geodynamic models of *Mittelstaedt et al.* [2008, 2011] demonstrated that this heating can substantially thin the lithosphere beneath hotspots on young (<5 Myr) seafloor, and could be the primary cause for numerous jumps of mid-ocean ridge segments to nearby hotspots evident in the geologic record. Large volumes of magmatic underplating beneath the volcanoes [*Watts & ten Brink* 1989] may also provide a substantial amount of heat in the shallow lithosphere. Mechanical weakening of the plate can occur by erosion of the walls of feeder dikes or the melting as magma penetrates the lithosphere. *Hieronymus & Bercovici* [2001] proposed that the fracture wall erosion can mitigate the lateral compressive stresses near the top of the lithosphere due to the upward curvature beneath volcanoes, thus allowing magma to penetrate the shallow lithosphere and erupt. In addition, the reduced compressive stress will reduce the effective flexural strength of the plate. We have not explored the effects of fracture wall erosion in our model.

Our preference for moderate thermal rejuvenation supports the idea that the Hawaiian swell is caused by combination of the isostatic effects of an anomalously hot geotherm and the dynamic effects of the buoyantly ascending plume material below the lithosphere [e.g., see *Ribe* 2004 and references therein]. The size of the isostatic effect can be estimated using the *Parsons & Sclater* [1977] plate cooling model. The difference between the isostatic seafloor depth over an anomalous 60-70 Myr geotherm and a 90 Myr geotherm is ~0.77-0.98 km. This suggests that the isostatic effect of lithosphere heating is ~45-65% of the total swell topography of 1.5-1.7 km along the axis of the Hawaiian Ridge [*Wessel* 2016].

Finally, in regards to rheology, the flow laws that produced the weakest lithosphere in this study and thus resulted in the highest posterior probabilities are *Kranjc et al.* [2016] and *Katayama & Karato* [2008]. The wet rheology of *Katayama & Karato* [2008], however, is not favored because there is no clear mechanism that allows water to penetrate and saturate large volumes of lithosphere at a hotspot. We thus favor the dry rheology of *Kranjc et al.* [2016]. Further study is needed to test whether *Kranjc et al.* [2016] provides a good fit elsewhere on the Pacific plate, but *Hunter & Watts's* [2016] analysis of *Mei et al.'s* [2010] rheology suggest that the ~2.7 magnitudes of weakening in *Kranjc et al.* [2016] could approximately explain the T_e values of the circum-Pacific subduction zones.

APPENDIX

Deformation of the oceanic lithosphere occurs primarily in four regimes [*Kohlstedt et al.* 1995], listed here in order of increasing temperature and thus depth:

(1) Frictional sliding, or the brittle regime, dominates the shallow, low-temperature lithosphere. Byerlee's law defines the relation between shear strength τ and normal stress σ_n,

$$\tau = \mu_f \sigma_n + C_f \, , \qquad (A.1)$$

where μ_f is the coefficient of friction, and C_f is frictional cohesive strength. Laboratory-derived values estimate a range for μ_f between 0.6 and 0.85 [*Byerlee* 1978]. Byerlee's law is incorporated into the Mohr-Coulomb theory for brittle failure, which causes the rate of increase in brittle strength with depth to be greater when the horizontal normal stress is compressive (negative differential stress) and less when the horizontal normal stress is tensile (positive differential stress) (Figure 3). Also, the weight of a 5-km-thick water column is assumed to add to σ_n and thus the brittle strength at the surface of the lithosphere.

(2) The semi-brittle regime begins at the brittle-ductile transition. This transitional regime begins when the plastic flow strength is approximately five times the frictional strength, and ends when brittle deformation is no longer possible and low-temperature plasticity becomes the dominant deformation method [*Kohlstedt & Mackwell* 2009]. The brittle-plastic transition occurs when the confining pressure becomes greater than differential stress ($\sigma_1 - \sigma_3 < P_m$), called the Goetze criterion [*Mei et al.* 2010]. Semi-brittle

deformation is poorly understood because it is difficult to simulate the conditions necessary to explore this regime, and so laboratory data are limited.

      (3) Low-temperature plasticity generally occurs between ~400°C-800°C. Dislocation glide in the crystalline lattice causes plastic deformation, limited by the lattice's resistance to dislocation movement. The lattice resistance, quantified as Peierls stress (σ_p), is large for mantle minerals that are covalent or ionic-covalent solids, such as olivine [*Mei et al.* 2010]. The general form of the flow law that describes low-temperature plasticity is

$$\dot{\varepsilon} = AF\sigma^r \exp\left[\frac{-E_k(0)}{RT}\left(1 - \left(\frac{\sigma}{\sigma_p}\right)^p\right)^q\right], \tag{A.2}$$

where A is a pre-exponential parameter, F is our added weakening factor; p, q, and r are dimensionless constants that depend on the energy barriers to dislocation motion; $E_k(0)$ is zero-stress activation energy; R is the gas constant; and $\dot{\varepsilon}$ is strain rate. Numerical values for these parameters are derived in the laboratory by steady-state deformation experiments (such as those using a D-DIA apparatus) or using nanoindentation [e.g., *Mei et al.* 2010; *Kranjc et al.* 2016].

Table A.1: Parameter values for the low-temperature plasticity flow laws tested; see Eq. A.2 for flow law format. *Boioli et al.* [2015] uses creep activation enthalpy Q and Boltzmann's constant k_b in lieu of zero-stress activation energy $E_k(0)$ and gas constant R and contains a coefficient of 2 before the Peierls stress term.

	A (s^{-1} Pa^{-2})	r	$E_k(0)$ or Q	σ_p (x 10^9 Pa)	p	q
Mei et al. [2010]	1.4 x 10^{-19}	2	320 kJ/mol	5.9	0.5	1
Kranjc et al. [2016]	7.09 x 10^{-17}	2	320 kJ/mol	5.4	0.5	1
Boioli et al. [2015]	5.07 x 10^7	0	5.4 eV	1.73 x 2	0.5988	1.1506
Katayama & Karato [2008]	6.31 x 10^{-5}	2	518 kJ/mol	2.87	1	2

      (4) High-temperature (plastic) creep occurs at temperatures >~800°C, at significantly lower stresses than low-temperature plasticity [*Mei et al.* 2010]. Dislocation and diffusion creep dominate deformation at this regime. The power law for high-temperature creep is expressed as

$$\dot{\varepsilon} = B\sigma^n \exp\left[\frac{-E^* + PV^*}{RT}\right], \tag{A.3}$$

where B is a material-dependent parameter (1.1 x 10^{-5} s^{-1}MPa^{-n} for dry olivine); E^* is creep activation energy (530 kJ/mol); V^* is activation volume (14 x 10^{-6} m3/mol); P is pressure, which is depth-dependent; n is a dimensionless constant. For dislocation creep, we use $n = 3.5$ [*Hirth & Kohlstedt* 2003].

REFERENCES

Ballmer, M.D., Ito, G., van Hunen, J., and Tackley, P.J. (2011), Spatial and temporal variability in Hawaiian hotspot volcanism induced by small-scale convection. *Nat. Geosci.*, 4, 457-460.

Ballmer, M.D., Ito, G., Wolfe, C.J., and Solomon, S.C. (2013), Double layering of a thermochemical plume in the upper mantle beneath Hawaii. *Earth Planet. Sci. Lett.*, 376, 155-164.

Becker, J.J., Sandwell, D.T., Smith, W.H.F., Braud, J., Binder, B., Depner, J., Fabre, D., Factor, J., Ingalls, S., Kim, S-H., Ladner, R., Marks, K., Nelson, S., Pharaoh, A., Trimmer, R., Von Rosenberg, J., Wallace, G., and Weatherall, P. (2009), Global Bathymetry and Elevation Data at 30 Arc Seconds Resolution: SRTM30_PLUS. *Marine Geodesy*, 32, 355-371.

Boioli, F., Tommasi, A., Cordier, P., Demouchy, S., and Mussi, A. (2015), Low steady-state stresses in the cold lithosphere mantle inferred from dislocation dynamics models of dislocation creep in olivine. *Earth Planet. Sci. Lett.*, 432, 232-242.

Byerlee, J. (1978), Friction of Rocks. *Pure Appl. Geophys.*, 116, 615-626.

Calmant, S. (1987), The elastic thickness of the lithosphere in the Pacific Ocean. *Earth Planet. Sci. Lett.,* 85, 277-288.

Carlson, R.L., Snow, K.R., and Wilkens, R.H. (1988), Density of old oceanic crust: an estimate derived from downhole logging on ODP Leg 102. *Proc. Ocean Drill. Prog. Sci. Results*, 102, 63-68.

Carlson, R.L., and Raskin, G.S. (1984), Density of the ocean crust. *Nature*, 311, 555-558.

DeLaughter, J.E., Stein, C.A., and Stein, S. (2005), Hotspots: a view from the swells, in *Plates, Plumes, and Paradigms*, edited by Foulger, G.R., Natland, J.H., Presnall, D.C., and Anderson, D.L. *Geol. Soc. Amer. Spec. Pap.*, 388, 257-278.

DeLaughter, J., Stein, S., and Stein, C. (1999), Extraction of the lithospheric aging signal from satellite geoid data. *Earth Planet. Sci. Lett*, 174, 173-181.

Demouchy, S., Mussi, A., Barou, F., Tommasi, A., and Cordier, P., (2014), Viscoplasticity of polycrystalline olivine experimentally deformed at high pressure and 900°C. *Tectonophysics*, 623, 123-135.

Demouchy, S., Tommasi, A., Boffa Ballaran, T., Cordier, P. (2013), Low strength of Earth's uppermost mantle inferred from tri-axial deformation experiments on anhydrous olivine crystals. *Phys. Earth Planet. Inter.*, 220, 37-49.

Detrick, R.S., and Crough, S.T. (1978), Island subsidence, hot spots, and lithospheric thinning. *J. Geophys. Res.* **83**(B3), 1236-1244

Evans, B., and Goetze, C. (1979), The temperature variation of hardness of olivine and its implication for polycrystalline yield stress. *J. Geophys. Res.* **84**(B10), 5505-5524.

Ghosh, A., Holt, W.E., and Wen, L. (2013), Predicting the lithospheric stress field and plate motions by joint modeling of lithosphere and mantle dynamics. *J. Geophys. Res.*, 118, 346-368.

Goetze, C., (1978), The mechanisms of creep in olivine, *Phil. Trans. R. Soc. Lond. A, Math. Phys. Sci.*, **288**(1350), 99-119.

Harris, R.N., and McNutt, M.K. (2007), Heat flow on hot spot swells: Evidence for fluid flow. *J. Geophys. Res.*, 112, B03407.

Harris, R.N., Garven, G., Georgen, J., McNutt, M.K., Christiansen, L., and Von Herzen, R.P. (2000), Submarine hydrogeology of the Hawaiian archipelagic apron – 2. Numerical simulations of coupled heat transport and fluid flow. *J. Geophys. Res.*, **105**(B9), 21,371-21,385.

Hieronymus C.F., and Bercovici, D. (2001), Focusing of Eruptions by Fracture Wall Erosion. *Geophys. Res. Lett.*, 28, 1823-1826.

Hirth, G., and Kohlstedt, D. (2003), Rheology of the Upper Mantle and the Mantle Wedge: A View from the Experimentalists, in *Inside the Subduction Factory,* edited by Eiler, J. American Geophysical Union*, 83-105.

Hunter, J., and Watts, A.B. (2016), Gravity anomalies, flexure and mantle rheology seaward of circum-Pacific trenches. *Geophys. J. Int.*, 207, 288-316.

Kalnins, L.M., and Watts, A.B. (2009), Spatial variations in effective elastic thickness in the Western Pacific Ocean and their implications for Mesozoic volcanism. *Earth Planet. Sci. Lett.*, 286, 89-100.

Katayama, I., and Karato, S. (2008), Low-temperature, high-stress deformation of olivine under water-saturated conditions. *Phys. Earth Planet. Int.*, **168**(3), 125-133.

Kohlstedt, D.L., Evans, B., and Mackwell, S.J. (1995), Strength of the lithosphere: Constraints imposed by laboratory experiments. *J. Geophys. Res.*, **100**(B9), 17,587-17,602.

Kohlstedt, D.L., and Mackwell, S.J. (2009), Strength and deformation of planetary lithospheres, in *Planetary Tectonics*, edited by Waters, T. and Schultz, R. Cambridge Univ. Press, New York. 395-455.

Kranjc, K., Rouse, Z., Flores, K.M., and Skemer, P. (2016), Low-temperature plastic rheology of olivine determined by nanoindentation. *Geophys. Res. Lett.*, **43**(1), 176-184

Laske, G., Markee, A., Orcutt, J.A., Wolfe, C.J., Collins, J.A., Solomon, S.C., Detrick, R.S., Bercovici, D., and Hauri, E.H. (2011), Asymmetric shallow mantle structure beneath the Hawaiian Swell—evidence from Rayleigh waves recorded by the PLUME network. *Geophys. J. Int.*, 187, 1725-1742.

Li, X., Kind, R., Yuan, X., Wölbern, I., and Hanka, W. (2004), Rejuvenation of the lithosphere by the Hawaiian plume. *Nature*, 427, 827-829.

Lowry, A.R., and Smith, R.B., (1995), Strength and rheology of the western U.S. Cordillera. *J. Geophys. Res.*, **100**(B9), 17,947-17,963.

MacDonald, G.A., Abbott, A.T., and Peterson, F.L. (1983), *Volcanoes in the Sea: The Geology of Hawaii*. 517 pp., Univ. of Hawaii Press, Honolulu.

McNutt, M.K., and Menard, H.W. (1982), Constraints on yield strength in the oceanic lithosphere derived from observations of flexure. *Geophys. J. R. Astr. Soc.*, 71, 363-394.

Mei, S., Suzuki, A.M., Kohlstedt, D.L., Dixon, N.A., and Durham, W.B. (2010), Experimental constraints on the strength of the lithospheric mantle. *J. Geophys. Res.*, 115, B08204.

Mittelstaedt, E., Ito, G., and Behn, M.D. (2008), Mid-ocean ridge jumps associated with

hotspot magmatism. *Earth Planet. Sci. Lett.*, 266, 256-270.

Mittelstaedt, E., Ito, G., and van Hunen, J. (2011), Repeat ridge jumps associated with plume ridge interaction, melt transport, and ridge migration. *J. Geophys. Res.*, 116, B01102.

Moore, W.B., Schubert, G., and Tackley, P. (1998), Three-Dimensional Simulations of Plume Lithosphere Interaction at the Hawaiian Swell. *Science*, 279, 1008-1011

Müller, R.D., Sdrolias, M., Gaina, C., and Roest, W.R. (2008), Age, spreading rates and spreading symmetry of the world's ocean crust. *Geochem. Geophys. Geosyst.*, 9, Q04006.

O'Connor, J.M., Steinberger, B., Regelous, M., Koppers, A.A.P., Wijbrans, J.R., Haase, K.M., Stoffers, P., Jokat, W., and Garbe-Schönberg, D. (2013), Constraints on past plate and mantle motion from new ages for the Hawaiian-Emperor Seamount Chain. *Geochem. Geophys. Geosyst.*, **14**(10), 4564-4584.

Parker, R. L. (1972), The rapid calculation of potential anomalies. *Geophys. J. R. Astron. Soc.*, 31, 447-455.

Parmentier, E.M., and Haxby, W.F. (1986), Thermal Stresses in the Oceanic Lithosphere: Evidence from Geoid Anomalies at Fracture Zones. *J. Geophys. Res.*, **91**(B7), 7193-7204.

Parsons, B., and Sclater, J.G. (1977), An analysis of the variation of ocean floor bathymetry and heat flow with age. *J. Geophys. Res.*, **82**(5), 803-827.

Raterron, P., Wu, Y., Weidner, D.J., and Chen, J. (2004), Low-temperature olivine rheology at high pressure. *Phys. Earth Planet. Int.*, **145**(1), 149-159.

Ribe, N.M. (2004), Through thick and thin. *Nature*, 427, 793-795

Ribe, N.M., and Christensen, U.R. (1994), Three-dimensional modeling of plume-lithosphere interaction. *J. Geophys. Res.*, **99**(B1), 669-682.

Ritzwoller, M.H., Shapiro, N.M., and Zhong, S.J. (2004), Cooling history of the Pacific lithosphere. *Earth Planet. Sci. Lett.*, 226, 69-84.

Sandwell, D.T. (1984), Thermomechanical evolution of oceanic fracture zones. *J. Geophys. Res.*, **89**(B13), 11,401-11,413.

Sandwell, D. T., Müller, R. D., Smith, W. H. F., Garcia, E., and Francis, R. (2014), New global marine gravity model from CryoSat-2 and Jason-1 reveals buried tectonic structure. *Science*, **346**(6205), 65-67.

Schmerr, N. (2012), The Gutenberg Discontinuity: Melt at the Lithosphere-Asthenosphere Boundary. *Science*, **335**(6075), 1480-1483.

Smith J.R., and Kelley C.D. (2010) Multibeam Synthesis of the Northwestern Hawaiian Islands Supports Diverse Research in the Papahānaumokuākea Marine National Monument. *Abstract OS13C-1240 presented at 2010 Fall Meeting, AGU, San Francisco.* 13-17 Dec, 2010. http://www.pacioos.hawaii.edu/metadata/hurl_bathy_60m_nwhi.html

Main Hawaiian Islands Multibeam Bathymetry and Backscatter Synthesis. 20 Nov, 2014. http://www.soest.hawaii.edu/HMRG/multibeam/

Stein, C., and Stein, S. (1992), A model for the global variation in oceanic depth and heat flow with lithospheric age. *Nature*, 359(6391), 123-129.

Timoshenko, S., and Woinowsky-Krieger, S. (1959), *Theory of Plates and Shells*, 580 pp., McGraw-Hill, New York.

Turcotte, D., and Schubert, G. (2014), *Geodynamics*. 623 pp., Cambridge Univ. Press, Cambridge.

Von Herzen, R.P., Cordery, M.J., Detrick, R.S., and Fang, C. (1989), Heat flow and the thermal origin of hot spot swells: The Hawaiian Swell revisited. *J. Geophys. Res.*, 94(B10), 13,783-13,799.

Von Herzen, R.P., Detrick, R.S., Crough, S.T., Epp, D., and Fehn, U. (1982), Thermal origin of the Hawaiian swell: Heat flow evidence and thermal models. *J. Geophys. Res.*, **87**(B8), 6711-6723.

Watts, A.B. (1978), An Analysis of Isostasy in the World's Oceans – 1. Hawaiian-Emperor seamount chain. *J. Geophys. Res.*, **83**(B12), 5989-6004.

Watts, A. B. (2001), *Isostasy and Flexure of the Lithosphere*. 458 pp., Cambridge Univ. Press, Cambridge.

Watts, A.B., and ten Brink, U.S. (1989), Crustal Structure, Flexure, and Subsidence History of the Hawaiian Islands. *J. Geophys. Res.*, **94**(B8), 10,473-10,500.

Watts, A.B., and Zhong, S. (2000), Observations of flexure and the rheology of the lithosphere. *Geophys. J. Int.*, **142**(3), 855-875.

Watts, A.B., Zhong, S.J., and Hunter, J. (2013), The Behavior of the Lithosphere on Seismic to Geologic Timescales. *Annu. Rev. Earth Planet. Sci.*, 41, 443-468.

Wessel, P. (1993), A Reexamination of the Flexural Deformation Beneath the Hawaiian Islands. *J. Geophys. Res.*, **98**(B7), 12,177-12,190.

Wessel, P. (1998), An Empirical Method for Optimal Robust Regional-Residual Separation of Geophysical Data. *J. Math. Geol.*, **30**(4), 391-408.

Wessel, P. (2016), Regional-residual separation of bathymetry and revised estimates of Hawaii plume flux. *Geophys. J. Int.*, 204, 932-947.

Wessel, P., and Haxby, W.F. (1990), Thermal stresses, differential subsidence, and flexure at oceanic fracture zones. *J. Geophys. Res.*, **95**(B1), 375-391.

Wessel, P., Smith, W.H.F., Luis, J.F., and Wobbe, F. (2013), Generic Mapping Tools: Improved version released. *EOS Trans. AGU*, 94, 409-410.

Wolfe, C.J., Solomon, S.C., Laske, G., Collins, J., Detrick, R.S., Orcutt, J.A., Bercovici, D., and Hauri, E.H. (2009), Mantle Shear-Wave Velocity Structure Beneath the Hawaiian Hot Spot. *Science*, 326, 1388-1390.

Zhong, S., Watts., A.B. (2013), Lithospheric deformation induced by loading of the Hawaiian Islands and its implications for mantle rheology. *J. Geophys. Res.*, **118**(11), 1105-1111.